Article

An Attempt to Construct an Activity Cycle Catalog with Kepler Long-Cadence Light Curves

Yu-Fu Shen [1,2], Gang Zhao [1,2,*] and Sarah A. Bird [1,3,4,5]

1   CAS Key Laboratory of Optical Astronomy, National Astronomical Observatories,
    Chinese Academy of Sciences, Beijing 100101, China
2   School of Astronomy and Space Science, University of Chinese Academy of Sciences, Beijing 100049, China
3   College of Science, China Three Gorges University, Yichang 443002, China
4   Center for Astronomy and Space Sciences, China Three Gorges University, Yichang 443002, China
5   Shanghai Astronomical Observatory, Chinese Academy of Sciences, 80 Nandan Road, Shanghai 200030, China
*   Correspondence: gzhao@nao.cas.cn

Abstract: Many stars show activity cycles like the Sun. Kepler has gathered ∼200,000 light curves. Most of the Kepler stars only have long-cadence light curves, which limits their applicable methods. Some metrics, for example S_{ph}, are effective for long-cadence light curves but require rotation periods. In order to improve the utilization of Kepler light curves, we introduce and use the smoothness metric. The smoothness metric is able to analyze stars without a measured rotation period and is applicable for long-cadence light curves. We test and validate our metric, resulting in the detection of the 11 years solar cycle and a 457 days cycle for our prototype star KIC 9017220. We analyze 92,084 Kepler long-cadence light curves, and as our main results, we detect 4455 magnetic activity cycle candidates, but about 20 percent are false cycles and 50 percent are lower limits of the real cycles, and we analyze their causes in detail. As an investigation into the performance of our method, we simulate disturbance factors and prove that the *p*-value test is invalid under certain circumstances.

Keywords: activity-stars; data analysis; statistics; photometric

1. Introduction

Magnetic activity cycles of a star can affect the climate of its planets, which is the case for the Sun and the Earth [1–3]. Cycles are also helpful to shed light on the origin of stellar magnetic fields [4–6]. It is thus advantageous to build a large statistical sample of the magnetic activity cycles of other stars besides the Sun.

Spots [7–10], X-ray emission (usually related to flares [11]), solar acoustic oscillation frequencies (p-modes [12–21]), Ca II H and K emission [22–24], brightness [25–27], etc., are stellar phenomena which are useful for determining the activity cycles of stars. Additionally, the Zeeman–Doppler effect can be used to determine stellar activity cycles directly [28].

Kepler light curves offer advantages to observing the signature of spots. Firstly, if the star rotates fast enough, the spots appear periodically in the field of view, and the light curve exhibits periodicity, which is called rotational modulation. Thus, the Kepler targets with confirmed rotation periods are appropriate samples to characterize spots and search for magnetic activity cycles in a similar manner as Reinhold et al. [29]. The variability range R_{var} [30] and S_{ph} [31] are metrics defined to characterize magnetic activity, and both have been used to estimate the magnetic activity of the Sun and solar-type stars [30,32–34]. A length of time needs to be defined in order to separate the light curve into segments to be used in the time series R_{var} or S_{ph} [35]. The length of the segments is fixed when calculating R_{var}, while the length is scaled to the rotation period when calculating S_{ph}. The segment of R_{var} is always set at about 30 days to 90 days, which provides 10 to 50 points along the time series for each Kepler target. Secondly, if the star rotates too slowly to cause rotational modulation, which means from birth to death a spot is always in sight, it will be hard to

distinguish a spot event from a transit event. Fortunately, when the spot is blocked by a planet, it will produce a slight increase in luminosity during a short period of the transit, which is reliable enough to characterize spots [36]. Based on this, Estrela and Valio [36] found activity cycles of two stars. However, the slight increase in luminosity lasts only several minutes. Kepler long-cadence light curves only provide two data points per hour, so this method can only be used on Kepler short-cadence light curves [8].

Kepler also has advantages in observing flares [37,38]. Detecting flares with an energy of less than 10^{34} erg is difficult with Kepler long-cadence light curves due to low time resolution [37]. In long-cadence light curves, most flares are detected as outliers in flux. The time series R_{var} and S_{ph}, mentioned above, are insensitive to flares because they neglect outliers in the stellar flux. In order to characterize magnetic activity by making use of the rejected outliers in the stellar light curves, we introduce a new method to select the outliers using the following steps. First, we smooth the light curve with a boxcar. A reliable length for the boxcar is about 8 h [39], this is called "F8". Then, we apply the smoothing filter by subtracting the light curve by the smoothing curve. Finally, we define the outliers as the data points which are larger than 3-sigma of the smoothed light curve. The outliers are possible candidates for solar activity such as flares and spots. We use the outliers to classify the roughness or smoothness of the light curve. Although there are still many unknown factors that could affect the smoothness, recently, the relationship between magnetic activity and the smoothness of light curves has been considered as relevant to magnetic activity [39–41]. We show that using outliers to characterize the smoothness cycle is a meaningful supplement to R_{var} and S_{ph} because the outliers neglected by R_{var} and S_{ph} are still relevant to the magnetic activity of a star. These outliers indicate that the related segments of the light curve are rough, which means the magnetic activity is strong at the corresponding time. When the outliers show a periodic distribution, we can define the "smoothness cycle" of the star. Considering that a few outliers could be caused by contamination and the values of the outliers always have higher errors, we introduce a metric which only focuses on the number of outliers and is insensitive to several false outliers.

The structure of the paper is as follows. The data selection is introduced in Section 2.1. The processes only necessary for Kepler data are introduced in Section 2.2. The method is introduced in Section 3.1. The method is used to find the 11 years smoothness cycle of the Sun from total solar irradiance (TSI [42]) data in Section 3.2. The disturbance factors we found when trying to construct an activity cycle catalog with Kepler targets are introduced in Section 3.3. The existence of cycles longer than the observational length of Kepler data is judged in Section 3.3.3. The cycle sequence is discussed in Section 4.1. The comparison with previous work is given in Section 4.2. The R_{var} and S_{ph} methods and our method are compared in Section 4.3. The *p*-value test is proved to be invalid in some cases in Section 4.4. Additional discussion is included in Section 4.5. A conclusion is given in Section 5.

2. Data

2.1. Data Selection

Kepler has taken ~4 years (exactly 1470 days) of repeated observations for ~200,000 targets [43]. Most targets have long-cadence (~30 min time resolution) light curves and some targets (less than 0.5 percent) have short-cadence (~1 min time resolution) light curves. Kepler data could in principle allow for the collection of a large number of activity cycles. The Kepler Pre-search Data Conditioning Module (PDC flux data (https://archive.stsci.edu/kepler/manuals/archive_manual.pdf, accessed on 1 May 2020) is organized by observing quarters because the spacecraft needs to rotate about its axis to keep the solar panel towards the Sun. A full-length quarter is ~90 days. A complete ~4 years Kepler long-cadence light curve should have 17 quarters. Not all quarters are full-length. In order to retain as large a sample as possible, we accept all light curves which are suitable for our metric. Out of 200,038 stellar light curves [44], we remove 2920 binaries [45] and 80,190 stars with two or more missing quarters (details in Section 2.2). This leaves 118,018 Kepler stellar light curves. Next, we consider light curves which

invalidate our smoothing filter by introducing false signals that are incorrectly interpreted as part of a stellar magnetic activity cycle. Transits, super flares, big spots, fast-rotating binaries, etc., may invalidate the method, especially when they have a time scale of 8 h or less (Section 3.1) and appear many times. Instrument modulations could lead to similar effects, too. Under these circumstances, false signals are selected by our method. On the one hand, some of these false signals (caused by transits, binaries, and instrument modulations) have no relationship with magnetic activity. They are obviously spurious detections which are not related to magnetic activity. On the other hand, super flares and big spots are incident cases and have a serious impact on the visible-band light curves. The false signals caused by super flares and big spots have a relationship with magnetic activity, but they are irregularly occurring events and not associated with regularly occurring magnetic activity cycles. Fortunately, our method is not sensitive to these false signals. False signals can be ignored when using our method, except for the case of egregious instrument modulations. Sometimes, the light curves are disturbed by instrument modulations and can be easily seen, but we cannot visually judge all light curves. To eliminate light curves that likely suffer from such instrument modulations, we added another criterion as follows: if more than three activity detections are selected in 0.5 days, and this appears more than 100 times, we eliminate the light curve from our final results (Section 2.2.1). Out of the 118,018 stars, 25,934 stars are removed, so there are 92,084 stars in our final sample. When using our method only on several specific targets, visual confirmation is an appropriate substitution to our added criteria, because visually, the instrument modulations are easily distinguished from the super flares and big spots. We do not sample according to the evolutionary stage of the stars. In this manner, our smoothness method allows for the inference of relationships between stellar structures and activity cycles.

We used KIC 9017220 to test our metric. KIC 9017220 is a main sequence star with a 15.292 days rotation period [46]. We selected KIC 9017220 for several technical reasons, which we discuss in Section 3.1.

We also used TSI data [42] to test our metric. TSI data are the total solar energy flux at 1 AU from the Sun (1 day time resolution). When using Kepler data, if we want to find the brightness cycle, we need to consider the effects of spots, rotation, and transits because we need to use the flux within a certain band to infer the total brightness. Spots have a large difference in different wavebands and may cause obvious rotational modulation, which would invalidate our method. We test the effects of spots when using Kepler data and discuss them in Section 3.1. When using our smoothness metric, the TSI data suffer from few false detections of solar magnetic activity, and we successfully measured the 11 years solar cycle (Section 3.2).

2.2. Pre-Processing Kepler Light Curves

Instrument modulation has a major impact on the flux of Kepler light curves. Pre-processing is required and introduces biases. Fortunately, our technique is insensitive to such biases because it concentrates just on outliers. The following is a brief introduction of the instrument modulation of Kepler. The amplitude of the brightness variations of the Kepler PDC light curve can change from quarter to quarter, which is not intrinsic to the star. One quarter corresponds to one charge-coupled-device (CCD) channel. Four CCD channels are used in rotation. The process to correct for instrument modulation is introduced in Section 2.2.1. Kepler PDC flux data are organized by several observing quarters because the spacecraft needs to rotate about its axis to keep the solar panel towards the Sun. The short breaks which exist between quarters as well as observed transits can result in "weak" discontinuity. Some Kepler targets have lost some quarters, which could result in "strong" discontinuity. Discontinuity is unavoidable in Kepler data. The impact of discontinuity is explained in Section 2.2.2.

2.2.1. Correction for Instrument Modulation

As introduced above, the amplitude of the brightness variations of the Kepler PDC light curve can change from quarter to quarter, which is not intrinsic to the star. When

visually examining a Kepler light curve, quarters look like rectangles with different widths at different heights. For convenience, we define the width of the rectangles to correspond to flux and the length to correspond to time. The Kepler data needs to be normalized and translated. He et al. [41] achieve this through the relative flux expression $\{x_t, t = 0, 1, \ldots, N - 1\}$ of the light curve:

$$x_t = \frac{X_t - \tilde{X}}{\tilde{X}}, \quad \tilde{X} = \text{median}(\{X_t\}). \tag{1}$$

Instrument modulations affect both $\tilde{X}$ and $X_t - \tilde{X}$, as indicated by their indirectly proportional relationship in Equation (1). However, for each of the four quarters, the coefficient of the proportional relationship between the impact on $\tilde{X}$ and the impact on $X_t - \tilde{X}$ may be different, and this difference becomes obvious when we connect all the quarters together into a ~4 years long light curve. The visual effect of this phenomenon is, in some targets, that some quarters are still wider than other quarters after obtaining the relative flux expression. To correct for this effect, the sigma value of each quarter is additionally calculated, and the data points are divided by sigma before the analysis. The sigma values are approximately proportional to the width of the rectangles, and they are used to normalize the different coefficients of the proportional relationship between the impact on $\tilde{X}$ and the impact on $X_t - \tilde{X}$ among different quarters. Afterwards, the light curve appears as an integrated rectangle instead of one rectangle for each quarter. This step removes the influence of instrument modulations caused by the CCD channels. We make note here of our selection criteria explained in Section 2.1, in which we remove light curves with serious instrument modulations. It is obvious to remove such light curves by visual judgement, but we have to set a criteria instead: if more than three activity detections are found in 0.5 days, and this appears more than 100 times, we eliminate the light curve from our final sample. As for the definition of activity detection, see Section 3.1.

2.2.2. Correction for Discontinuity in Kepler Light Curves

Kepler light curves are not completely continuous; the Kepler telescope sometimes rests, thus causing "weak" or "strong" discontinuity in the light curves.

The criterion mentioned at the last paragraph of Section 3.1 helps to exclude the effect of short breaks causing "weak" discontinuity. Short breaks are not only present between quarters but are also artificially created when transits appear in the light curve. The transits need to be filtered out by the smoothing operation when calculating the smoothness. However, when a transit event is less than 8 h, the "F8" smoothing filter is invalid (details discussed in Section 3.1). We remove sections of the light curve influenced by transits which are recorded in the NASA Exoplanet catalog (https://exoplanetarchive.ipac.caltech.edu/, accessed on 1 May 2020); this process artificially introduces short breaks into our light curve data. Preferably, the contour of the transits should be carefully fitted instead of removing the points. If the transit was caused by a planet, the contour could be perfectly characterized. For such fitting of transit contours, short cadence is required, and the fitting process requires more time than simply removing the corresponding section of the light curve. We thus prefer to remove sections of the light curve with transit candidates in order to.

To understand the impact of "weak" discontinuity, we use 8214 Kepler stars with transits recorded in the NASA Exoplanet catalog as a test sample. However, some of the 8214 stars may not have transits, and only about half of the transits are confirmed planets. We did not make a distinction because our purpose was to test the impact of "weak" discontinuity, as long as the short breaks are introduced. We did not find any relation between transits and the smoothness cycles, so we conclude that weak discontinuity has a limited effect on the result. Incidentally, we make another comparison. Some previous studies indicate that planets could possibly influence their host stars [47–50], which means, for example, the 11.8 years Jupiter orbital cycle and the 11 years solar cycle may have a physical relationship. As we find no relation between the smoothness cycles and planet transits, our results thus do not support this idea.

We apply separate criteria to eliminate the effects of the "strong" discontinuity caused by missing quarters. As mentioned in Section 1, Kepler PDC flux data are organized by observing quarters. A complete ~4 years Kepler long-cadence light curve should have 17 quarters. Almost half of the Kepler long-cadence light curves have 16 quarters or fewer. The missing quarters disrupt the continuity of the data seriously and change the sampling function. Our smoothness metric interprets the missing segment of the light curve as a lack of magnetic activity. The activity detection then sharply increases at the end of each missing quarter. Our smoothness metric detects a false periodic signal if this sharp increase happens more than once. To eliminate this effect of the "strong" discontinuity, we remove Kepler targets with fewer than 16 quarters (criteria listed in Section 2.1). If all the missing quarters are at the start or end of the light curve, the situation is better. During the initial testing of our method, we carefully choose appropriate targets. However, considering our large data set, such careful target selection costs extensive amounts of time, so we relaxed our target selection requirements during further testing. If only one quarter is missing, whether it is at the start, middle, or end of the light curve, we select the star as part of our final sample.

3. Method, Validation, and Results

3.1. Method

The goal of the smoothness metric is to locate the outliers, i.e. the light-curve data points with large deviations from the smoothing filter, which represent magnetic activity on the star in a light curve and check for periodicity, which represents a magnetic activity cycle. Each outlier can be seen as an activity detection. The outlying points appear to be outliers at the moment, but if the time resolution of the data improves, they may represent highly important physical processes.

Firstly, the light curve needs to be smoothed. We set a boxcar and choose the median of the data points in the boxcar as the smoothing filter. The final processed (smoothed) light curve is attained by subtracting this median from the raw light curve. This process for smoothing has been discussed by many previous works [39–41]. As for the size of the boxcar, an n hr boxcar measures stellar variability on time scales of n hours or less. If the length of time n is too large, our method cannot filter out disturbance factors. For example, if a star has a rotation period shorter than n hours and also has spots, the rotation period would be found instead of the smoothness cycle. Pulsation (change in the volume of stars which can lead to a change in flux, which may be caused by many factors and sometimes shows periodicity) can be mistaken as rotational modulation, and if the pulsation has a period shorter than n hours, the pulsation results in a false measurement using our metric. At different latitudes of a star, the spots have different rotation periods, which can cause beating patterns. When pulsation and rotational modulation coexist, beating patterns may also be produced. However, we can filter it out if the period of the beating patterns is longer than 8 hours. Overall, our metric does not require us to distinguish between rotational modulation and pulsation, nor does it require us to analyze the cause of beating patterns. Perhaps there are exceptions, but they are insignificant in such a large sample. When analyzing a small number of targets, extra attention needs to be made in order to investigate the impact of pulsations. The most important component of our metric is to choose the boxcar length that allows for the effective use of the smoothing filter. If a very small n value is chosen, the smoothing filter is assured to be effective, but if the n value is too small, our metric would filter out useful information. Ideally, each star should have an appropriately selected n value, but when analyzing large datasets such as those provided by Kepler, we simplify the method by applying the same value $n = 8\,\text{h}$ (Bastien et al. [39] termed this value as F8) to all analyzed light curves. In this study, 8 h is assumed to be suitable for most cases. To ensure the smoothing filter is appropriate, we add another criterion. If one side of the point in the middle of the boxcar has more points than the other side, and the difference is larger than two points, the middle point will be removed from the smoothed light curve before the analysis. Obviously, if the light-curve data are

equally spaced, this criterion will remove the first nine and the last nine data points only. The removed points still participate in the calculation of the median.

An example of the processed light curve is depicted in Figure 1. To illustrate the smoothing filter, Figure 2 provides a local enlargement of the left panel of Figure 1. The example taken is KIC 9017220, which we use as a prototype for our smoothness metric. Our metric classifies KIC 9017220 as a magnetic activity candidate and measures a 457 days activity cycle, which is similar to the short-cycle sequence as defined by Ferreira Lopes et al. [51]. For several technical reasons, we selected KIC 9017220 as a prototype. The light curve does not lack observational quarters and is easy to fit; the difference between its quarters is relatively small. Some specific pre-processing procedures only necessary for Kepler light curves are used on KIC 9017220. These procedures are discussed in detail in Section 2.2.
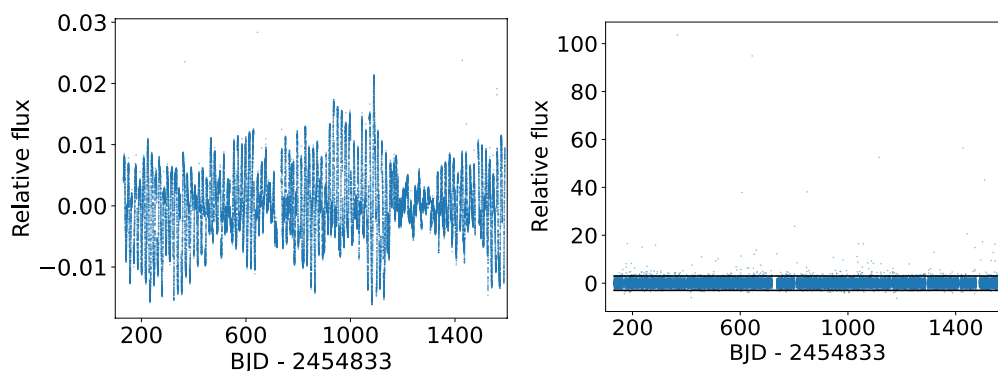
Figure 1. The left panel is the original light curve (after applying the pre-processing only necessary for Kepler as discussed in Section 2.2) and the right panel is the smoothed light curve after subtracting by the "F8" smoothing filter. The Kepler long-cadence PDC flux data used in both panels is from KIC 9017220. In the right panel, the two horizontal black lines represent the 3-sigma uncertainty range. In our smoothness metric, we define points $> \pm3$-sigma as outliers and then examine whether the outliers exhibit any periodicity.
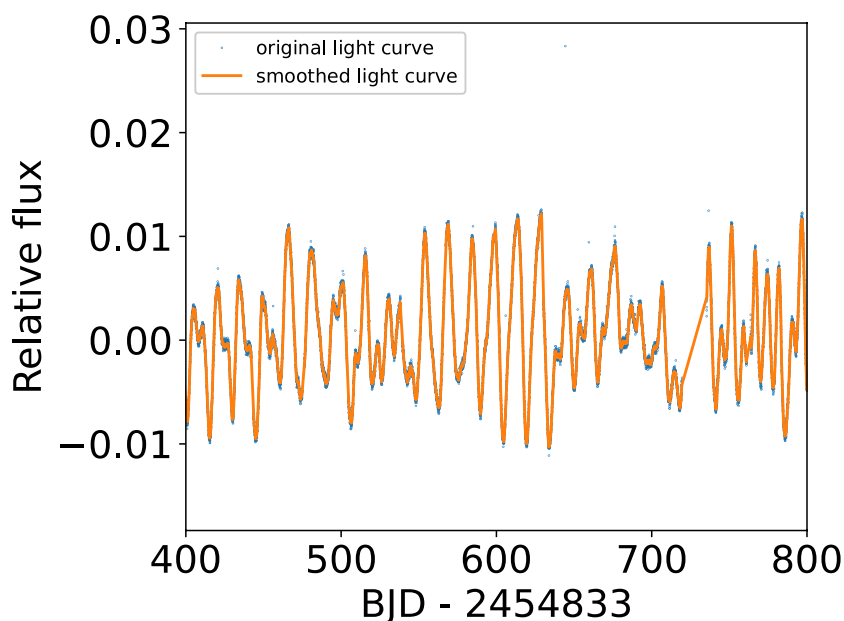
Figure 2. Kepler light curve for the star KIC 9017220. The full light curve and the full smoothed light curve are shown in Figure 1.

Secondly, we define the outliers as the light-curve data points which are $> \pm3$-sigma uncertainty range after applying the smoothing filter.

Thirdly, to exhibit the distribution of the points along the light curve more clearly and make the Lomb–Scargle periodogram easier to interpret, the number of outliers is summed and the total sum of the outliers vs. time is given (blue dots in the left panel of Figure 3). The relationship between the number of outliers and the time of observation is modeled by a line (the orange line in the left panel of Figure 3) when the outliers have a uniform distribution, signifying that the magnetic activity of the star is stable (shows no periodicity). We form the model line by connecting the first and last points of the number of outliers vs. the time diagram. The interpretation of such is that all the outliers appear at equal intervals.

We subtract the observed measured curve from the model line to attain the residuals, as shown in Figure 3 (right panel). We note that the stability of the outliers (no periodicity) does not mean the star is magnetically quiet; magnetically quiet stars show no outliers to detect.
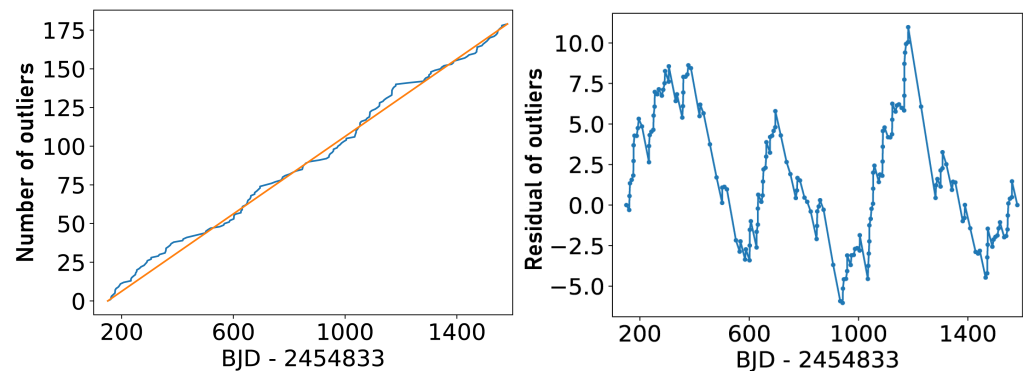
Figure 3. The left panel shows the total sum of the number of outliers vs. time for the observed light curve (blue) and an ideal line (orange) for detected magnetic activity during each observation. The line (orange) represents the uniform detection of magnetic activity. The right panel depicts the residuals from the line and the observed curve shown on the left. KIC 9017220 is taken as an example.

Lastly, we apply a Lomb–Scargle periodogram to the residuals (Figure 4). Fourier transformation of data with different time intervals requires special methods. In this work, we use the Lomb–Scargle periodogram. The essence of the Lomb–Scargle is to use the least squares method to fit sinusoidal functions; this is the most commonly used method to perform Fourier transformation on non-uniform signals. Then, we calculate the False Alarm Probability (FAP), or we can say, *p*-value. The *p*-value does not always have a unique definition. The *p*-value is the probability that a particular statistical measure of an assumed probability distribution is greater than or equal to (or less than or equal to in some instances) the observed results. Some statistical methods use a unique definition of the *p*-value. For example, the least squares method calculates chi-squared and attains a pre-tabulated *p*-value. Such tables are also available for the Lomb–Scargle periodogram. However, this *p*-value represents one single step. For our smoothing metric, there are many other steps, and we need the *p*-value of all the steps. The *p*-values of other steps cannot be calculated accurately; they can only be estimated using Monte Carlo simulations. The *p*-values of all steps as recovered by Monte Carlo simulations are always called FAP, but we also call it *p*-value in this work. In principle, we should calculate the series of *p*-values at each frequency because there may be more than one activity cycle, and the *p*-value series can give an uncertainty estimation of activity cycles. The selected band, i.e., the detection range of periodic signals, is set to longer than 1 day and shorter than 3000 days. In Reinhold et al. [29], the band is set to longer than 0.5 years and shorter than 6 years. The upper limit mainly depends on the length of the data series (light curve in this work), and the lower limit mainly depends on the sampling frequency (of the light curve in this work). If a cycle is longer than 6 years, due to the limiting length of the data, we may falsely measure the true cycle, but the detected existence of the cycle is reliable; we discuss this in detail in Section 3.3.3. As for the lower limit, our smoothness metric is able to provide more data points compared with other metrics because we rely on the outliers; thus, with

a larger sampling frequency, we expand the lower limit to 1 day. Our results show that most of the cycles we find are between 0.5 years and 6 years, similar to the band used by Reinhold et al. [29], as shown in Section 3.3.

The *p*-value is calculated by Monte Carlo simulation. First, we make a permutation by randomly selecting from the processed light curve the same number of points as the number of outliers measured. The number of outliers related to magnetic activity reaches around ~100 to ~1000 for each light curve in our sample of 92,084. Next, as in the previous step, we sum the number of outliers, subtract them from the model line, and attain the synthetic periodogram. Then, we subtract the synthetic periodogram from the real periodogram; the points greater than zero we set to one, and otherwise we set to zero. This gives an array of zeros and ones which has an equal length to the selected band. We compute 1000 random permutations and repeat the above steps, which yields 1000 arrays of zeros and ones. We add up the arrays of zeros and ones, then divide the array by 1000, which yields the *p*-value series. To improve computing efficiency, when analyzing the large number of Kepler targets, we only calculate the *p*-value of the strongest signal of each target. We accept light curves whose strongest signal has a *p*-value< 0.003 (3-sigma). If those cycles are confirmed, we calculate the total *p*-value series to determine the error range of those cycles. This *p*-value threshold is stricter than 0.05 as used by Reinhold et al. [29] due to the differences in our methods (as explained in the next paragraph).

In order to explain why we choose our limiting *p*-value as 0.003 instead of 0.05, we provide here a more detailed discussion of our *p*-value calculations. Once we have a synthetic periodogram, we make a comparison of the synthetic periodogram with the real periodogram. There are two ways to compare. The first way, after creating the permutations and obtaining the periodogram, only concentrates on the highest peaks of the synthetic periodograms. The second way compares the frequency of the real peaks with the same frequency of the synthetic periodograms. As opposed to Reinhold et al. [29], who used the former, we choose the latter. The description in the remainder of this paragraph explains our choice. The first way ignores the difference in the mistaken reporting rate between different frequency bands. Assuming we expand the frequency range to zero, the first way would be invalid because there is always an extremely high signal around zero frequency. However, the first way excludes more signals; therefore, by choosing the second, we need a stricter threshold.
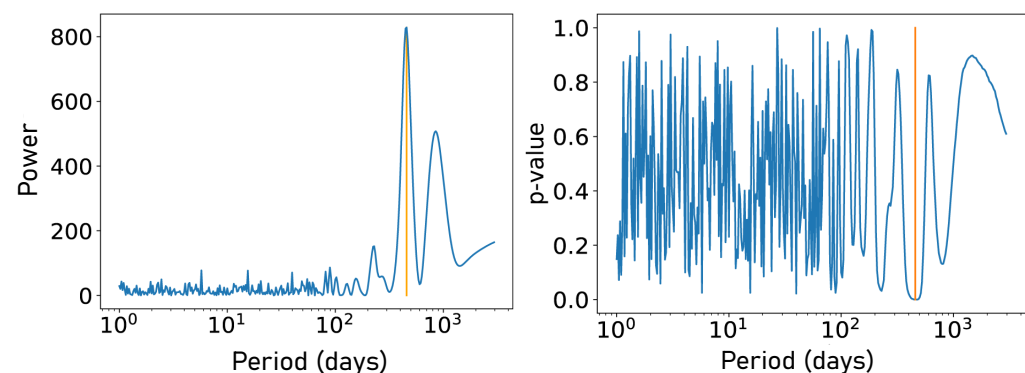
Figure 4. The left panel is the periodogram attained from the Fourier transformation of the residuals. The residuals are depicted in the right panel of Figure 3. A 457 days cycle is found. The right panel depicts the *p*-value of the left panel. The orange vertical lines in both panels mark the location of the cycle. KIC 9017220 is taken as an example.

3.2. Validation with TSI Data

The Sun is a slow rotator (about 25 days) and the rotational effect on the total solar energy flux data is weak, so we do not need to make any correction for such small rotational effects. Transits can also be ignored when using TSI data. The cadence additionally does not present large problems; the smoothing filter is always effective, such that we can choose the boxcar more freely, as long as we filter out the trend of total energy flux. The 11 years

solar brightness cycle is clearly seen in Figure 5a (green points). We select a 10 days boxcar and apply our smoothing metric. The smoothing line is shown in red in Figure 5a. The smoothed light curve is given in Figure 5b , such as in the right panel of Figure 1. The residual is given in Figure 5c , such as in the right panel of Figure 3. The power spectrum and the *p*-values are given in Figure 5d (a pair plots), such as in Figure 4. Then, we recover an 11 years smoothness cycle (the strongest peak in the periodogram, labeled in Figure 5d). Our smoothness metric detects more than one smoothness cycle for the Sun. Some of them may be harmonics, but some research indicates that the Sun may have several activity cycles with distinct sources [52]. These multiple detections allow us to determine the uncertainty of our detected cycles by making use of the colored horizontal lines in Figure 5d. It is meaningful to consider more than one cycle, but in this work, when analyzing Kepler data, we only consider the strongest cycle and leave the analysis of weaker samples for future work. Considering the 11 years solar cycle is a quasi-period, it is not important to discuss whether the two cycles are the same. The 11 years smoothness cycle we found only means that when the Sun is brighter; the brightness fluctuates more strongly. In other words, the cause of the increase in brightness and the cause of the brightness fluctuation occur either synchronously on the Sun or they are the same on the Sun. Since we cannot tell whether this is the same on other stars, it is necessary to treat smoothness as an independent factor.

(a)

(b)

(c)

Figure 5. *Cont.*

(**d**)
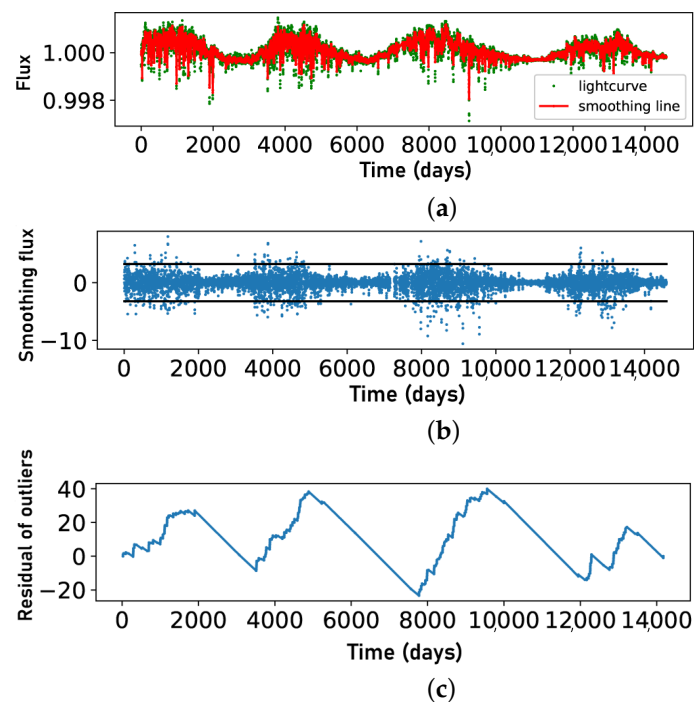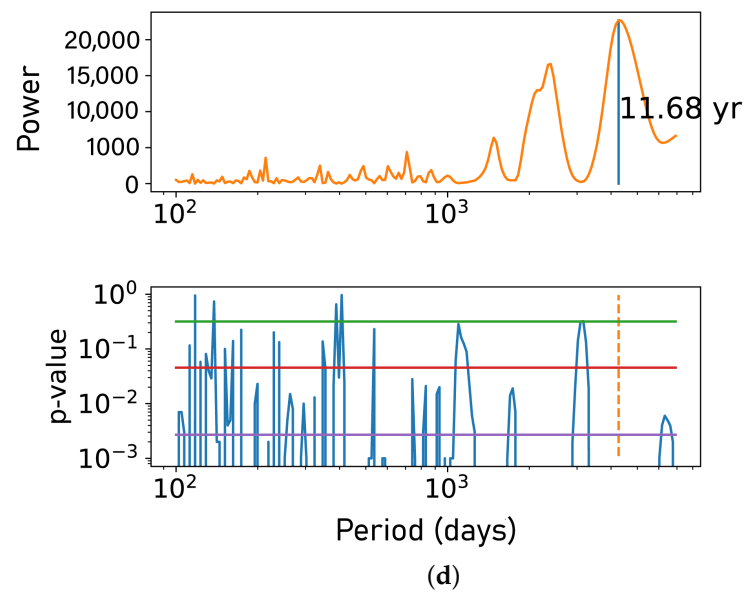
Figure 5. Panel (**a**) depicts the TSI data (green) and the smoothing line (red). Panel (**b**) depicts the light curve after subtracting the smoothing line (the smoothed light curve), and the two horizontal lines represent the 3-sigma range. Panel (**c**) depicts the residual between the summed number of outliers and the linear model representing constant magnetic activity. Panel (**d**) (a pair plots) contains the power spectrum and the *p*-values of panel (**c**). The green, red, and purple horizontal lines show the 1-sigma, 2-sigma, and 3-sigma uncertainty, respectively. The strongest cycle is marked in panel (**d**).

3.3. Result of the 92,084 Kepler Targets and the Disturbance Factors

After applying our smoothness metric to Kepler long-cadence light curves, we show our main results in Figure 6. We show the distribution of the smoothness cycle candidates detected by our smoothness metric. These cycles may represent magnetic activity cycles and are the Kepler candidates whose *p*-value is less than 0.003. From our 92,084 Kepler targets, we detect a total of 4455 candidates with likely magnetic activity cycles.

The distribution of cycle periods has at least four obvious peaks in Figure 6. Two peaks at about 1 year, one peak at about 2 years, and one peak at about 4 years. When we combine the two peaks that are about 1 year apart, we obtain three peaks in total. Part of those cycles corresponds to a real cycle but has been finitely shifted by the effect of the sampling function, which is explained in Section 3.3.1. Section 3.3.1 shows that the sampling function can explain the peak at ∼4 years and the location of the other peaks but cannot explain the height of the other peaks. Thus, other disturbance factors must be at work. We find that the CCD effect is correlated with the sampling function effect, and we explain this in detail in Section 3.3.2. Some cycles between 3 years and 6 years are actually longer cycles, which we discuss in Section 3.3.3.
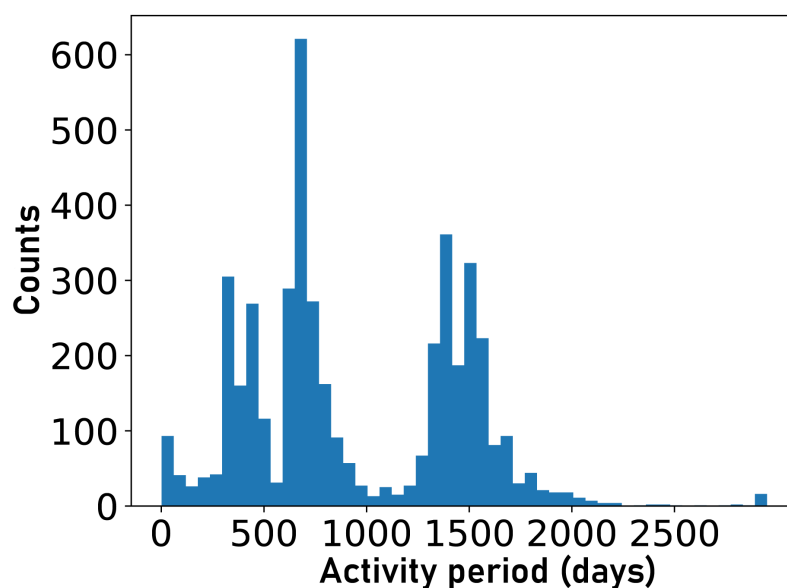
Figure 6. The distribution of Kepler activity cycle candidates found by our smoothness metric, which is defined as light curves whose strongest signal has a *p*-value < 0.003. Of the 92,084 Kepler light curves which we analyzed, 4455 pass our *p*-value test and are displayed in this figure.

3.3.1. Effect of the Sampling Function

The local maximums of the sampling function of a ∼4 years long data series and the several peaks in Figure 6 have a one-to-one correspondence. The impact of the sampling function needs to be considered. The application of a window function can partly offset the effects of the sampling function, but the discontinuity found in the Kepler long-cadence light curves is different from source to source; thus, selecting an appropriate window function is difficult. To further understand this effect, we conduct a Monte Carlo simulation.

To conduct the Monte Carlo simulation, we generated a synthetic light curve. A common way to generate a light curve is to add noise to a sine curve. When using our smoothing metric, the smoothing filter will filter out the sine function and only the noise remains. The application of our smoothness metric to synthetic light curves generated in this common way results equivalently to selecting the outlying points > 3-sigma from observed light-curve data. Although we use the more common and simpler method, we make note that Aigrain et al. [53] has investigated in depth the generation of more complex synthetic light curves. We generate periodically distributed outliers. In our following test of the impact due to the sampling function, we select a ∼4 years long portion of the periodically distributed synthetic light curve, measure the periodic signal, and compare this with the original synthetic cycle. We use synthetic data with an 800 days period as an example. Figure 7 shows the synthetic data and the ∼4 years segment that we randomly select. First we calculate the Lomb–Scargle periodogram for the whole synthetic light curve (upper panel of Figure 8). The location of the highest peak is not exactly 800 days. One reason for this is that the whole synthetic light curve is longer than 4 years but still finite. The second reason is that the cycle we generated is quasi-periodic; we simulate quasi-periodic data because the 11 years solar cycle is also quasi-periodic. Second, we randomly select a ∼4 years segment of the synthetic data and calculate the Lomb–Scargle periodogram (lower panel of Figure 8). Our smoothness metric detects the signal, but the signal is shifted. To further understand the effects of the finite length of the data (which represents the effect of the sampling function), we perform further tests. We simulate uniformly distributed periods in the range of 100-2000 days and apply our smoothness metric. We compare the distribution of the synthetic periods from the whole light curve with the distribution of the periods found by using a ∼4 years segment of the synthetic data. The results are depicted in Figure 9, which partly explains the peaks in Figure 6. The sampling function makes signals gather to the local maximum of the function, which could

explain why there are four peaks in Figure 6. If the effect of the sampling function is the only disturbance factor, we can calculate the uncertainty and perform a statistical analysis. Unfortunately, other disturbance factors exist. The height of the peaks in Figure 6 is still unexplained. We give some evidence to support the following idea in Section 3.3.2: the differences between the Kepler CCD channels can cause spurious cycles. We attempt to avoid problems due to the observing instruments by removing light curves with serious instrument modulations (Section 2.1) and by applying Equation (1) from Section 2.2.1.
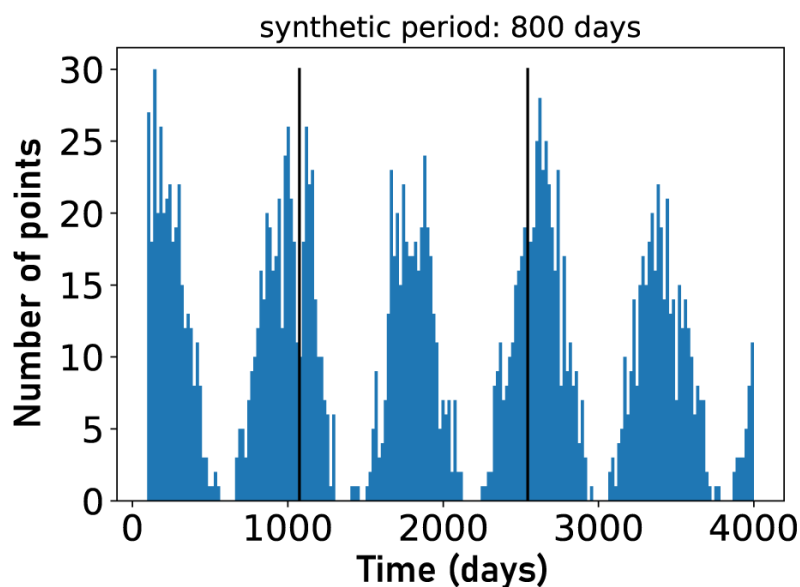
Figure 7. Example of periodically distributed synthetic outliers. We randomly select an ∼4 years segment (located between the two vertical black lines) for analysis.
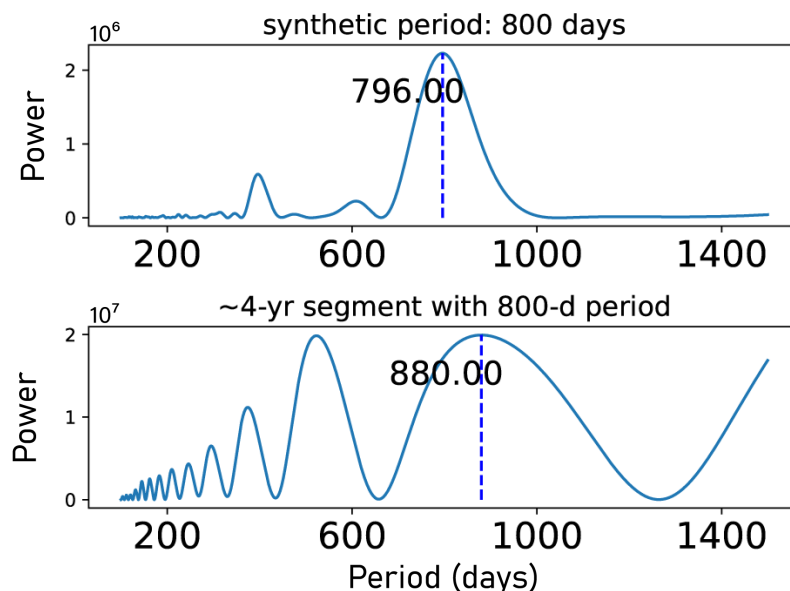
Figure 8. Power spectrum of the synthetic data points which are depicted in Figure 7. The upper panel depicts the periodogram of the total synthetic light curve. The lower panel depicts the periodogram of an ∼4 years (1470 days exactly) segment of the synthetic light curve. The peaks of both panels are marked by vertical dotted lines, and the positions of the peaks are given.
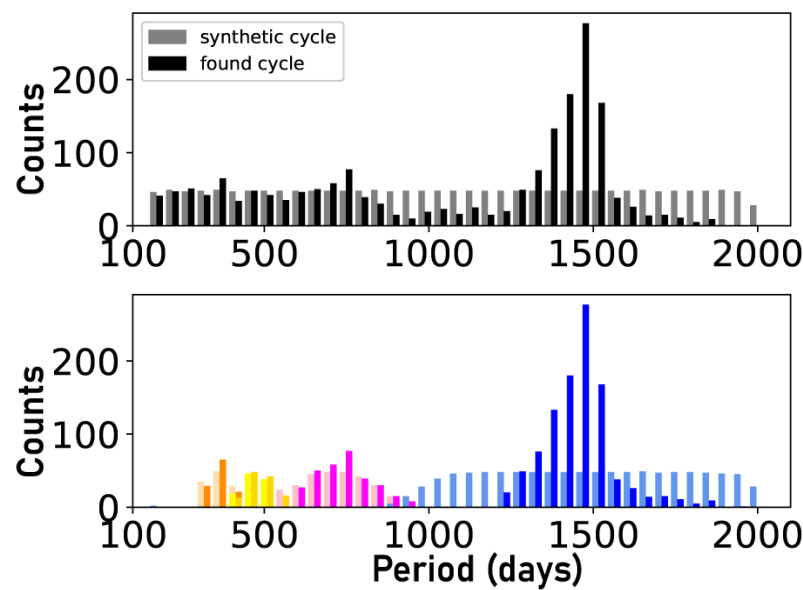
Figure 9. Both panels: lighter colors are the distribution of synthetic periods (input cycle) and darker colors are the output cycles recovered by our smoothness metric when applied to an ∼4 years segment. The top panel shows what will happen if the real cycles have a uniform distribution. The bottom panel is the same as the top, except the cycle periods staying in the same period bin have been excluded. The periods staying in the same period bin means that the input and output periods are in reasonable agreement. The four color pairs in the bottom panel highlight the peaks in the top panel.

3.3.2. Difference between Kepler CCD Channels as a Cause of Spurious Periods

The Kepler satellite has a 1 year orbital period. Every Kepler target is observed by four CCD channels in rotation. Most of the CCD channels last 90 days (a full-length quarter). Even if one of the CCD channels fails, it is detected as an ∼1 year cycle. If the CCD effect is weak and the ∼1 year cycle is not obvious, it may be identified as an ∼2 years cycle. The rotation of the CCD channels, thus, may be the source of the abnormal ∼1 year and ∼2 years cycles. To prove this, we count the CCD numbers of all Kepler targets and calculate the original proportions of the CCDs. Next, we calculate the proportions of the CCDs in the peaks. We compare the proportion of the CCDs in the peaks to the original proportion. Since we accept small differences in the proportions of the CCDs in the peaks compared with the original proportions, we perform a new Monte Carlo simulation to determine the range of differences, which we can accept and still retain accurate results. Firstly, we set an original proportion and generate random numbers between zero and one. If the number is less than the proportion, it is seen as a positive event. Secondly, we repeat this 4455 times and calculate the real proportion of positive events and perform this 1000 times to attain a distribution of real proportions. Thirdly, we calculate the sigma of the real proportions and set the 3-sigma range as the acceptable range. We perform the above steps in different original proportions. Figure 10 depicts the result. The black dots with error bars show the acceptable 3-sigma statistical range. The multicolored markers (each colored marker indicates a periodic cycle range as shown in the legend) represent the real proportions of the targets with a cycle found by our smoothness metric. One point has a very large deviation. This point corresponds to CCD channels 41 42 43 44, and this proportion is of the targets with cycles between 260 days and 500 days. The point with a very large deviation indicates the CCD channels 41 42 43 44 are the main disturbance factors causing the peak at about 1 year in Figure 6.

Due to the nature of our smoothness metric, several additional uncertainties are introduced due to the CCD channels, which can influence our detection of magnetic activity cycles. We select the outliers (the light-curve data points with large deviations from the smoothing filter) in order to measure the smoothness of the light curve. If one CCD channel erroneously produces multiple false data points with large deviations from the true light

curve, our metric would detect this as a 1 year cycle. Another possible source of uncertainty due to the CCD channel is self-noise. If one CCD channel produces more noise than the others, our metric may detect the increased noise as data points with large deviations and cause a spurious ~1 year period detection. Despite these possible explanations of false 1 year periods, the height of the peak at ~2 years is still unexplained. Considering a 1 year cycle can be detected as a 2 years cycle due to spurious shifts in the measured period, the peak at about 2 years may also be affected by the CCD effect. Kepler has an important interruption: safe-mode. If the self-noise of a CCD changes after a safe-mode event, there should be a ~2 years cycle. Moreover, unknown instrumental effects are possible, which can introduce 2 years false signals.

Unfortunately, we cannot describe the CCD effect precisely, so we cannot distinguish the spurious periods from the real cycles. Our results cannot be used for any statistical analysis. We can solve this problem by binning the data points before the analysis. The bigger the bin size chosen, the smaller will be the effect due to the CCD. However, a bigger bin size also means fewer data points, and the leakage effect would be more serious, so we do not choose to bin the data points. We further elaborate upon the leakage effect in the discussion. A preliminary estimate based on Figures 6 and 9 indicates that three-quarters of the 1 year and 2 years cycles are erroneous detections, or roughly twenty percent of the total. Although the CCD effect has not been solved yet, it is still helpful for us to confirm the cycles we found, which means, if the more active part could span quarters (a CCD corresponds to a quarter), it is more likely to be a true cycle. Figures 1–4 provide an example: KIC 9017220.
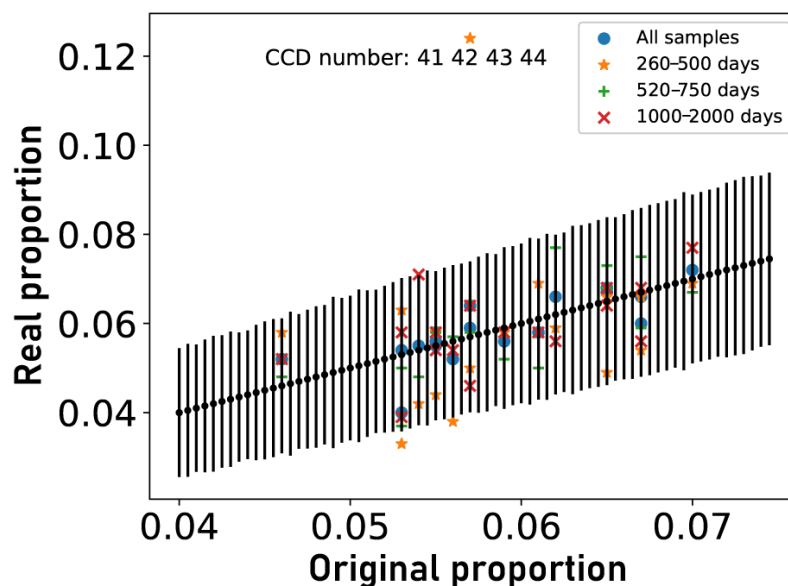
Figure 10. The horizontal coordinate represents the proportion of a CCD sequence to all targets, whereas the vertical coordinate represents the proportion of the same CCD sequence to targets for which a range (shown in the legend) of activity cycles was discovered. The black dots with error bars represent the allowable statistical range (3-sigma). If this range is exceeded, it indicates that the activity cycles within a given range (shown in the legend) are related to the relevant CCD sequence. Three points in the image fall beyond 3-sigma, all of which correspond to cycles of 1 year. One point is obviously abnormal, which corresponds to CCD channels 41 42 43 44 of the cycles between 260 days and 500 days.

3.3.3. Results for Determination of Longer Cycles

The existence of longer cycles (>4 years, the length of time for which Kepler observed) could affect the distribution of magnetic activity cycles detected by our smoothness metric. First, we select some 4 years TSI data segments for testing. As indicated in Figure 11, a signal is identified if there is a portion of the selected 4 years segment with significant activity change;

if there is little activity change during the 4 years segment, there is no signal. This test gives indications that, when there is a period longer than 4 years, the probability of finding a signal using a 4 years segment is the probability that the light curve segment contains a portion with a significant change in activity, i.e., the probability of locating a long activity cycle may be proportional to the phase of the selected segment. With only a 4 years sample, it is difficult to determine the phase, so we can only estimate the probability. So, we perform Monte Carlo simulations to investigate the effects of stellar magnetic activity cycles >4 years. Similar to our test in Section 3.3.1, we generate periodically distributed outliers randomly, and here, we select periods > 6 years. We analyzed a 4 years segment of the simulated light curve and checked for periodic signals that pass our *p*-value test. We performed 100 tests for each input period. We found that the shorter the input period, the higher the probability of finding a reliable signal. Figure 12 depicts the probability of finding a signal. Some tests are given as examples in Figure 13. Within our sample of stars, which we analyze from the Kepler catalog, is HD 173701 (KIC 8006161), which has a 2706 days cycle found by Karoff et al. [54] using a complete set of observations. Using our smoothness metric, we measure a 1905 days activity cycle for this star. The 2706 days (7.4 years) cycle is much longer than the Kepler mission (observations lasted ∼4 years). Despite this, our tests show that our smoothness metric is able to detect that an activity cycle exists (Figure 12). As Figure 12 shows, when the input period for our test is 7.4 years, the probability of detecting an activity cycle is very close to 1.0. Figure 12 explains why and how longer cycles can affect our results. As another example, we mention that a 40 years input period still has about 50 percent probability to be detected as an activity cycle within the 4 years segments used for our smoothness metric. Figure 12 shows that our smoothness metric is able to detect the existence of longer stellar cycles, albeit our determined cycle length is underestimated for cycles longer than 4 years. All the detected cycles around 4 years in Figure 6 are likely to be lower limits of the real cycle, which means about 50 percent of all activity cycles are possibly lower limits. Some ∼2 years cycles may also be coupled with longer cycles and CCD effects.

Note that our test may not reflect reality accurately. In terms of amplitude, if the signal's periodicity is perfect, the outcome is the same regardless of the cycle's amplitude. However, the signal cannot be perfect since the magnetic activity is quasi-periodic; hence, the larger the amplitude of the signal, the easier it is to identify the signal. There is no assurance that the quasi-periods derived from our simulations correspond to the actual situation. Nevertheless, we think the pattern identified by our test is qualitatively accurate.

(a)
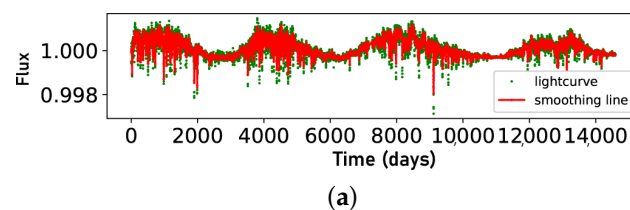
Figure 11. *Cont.*
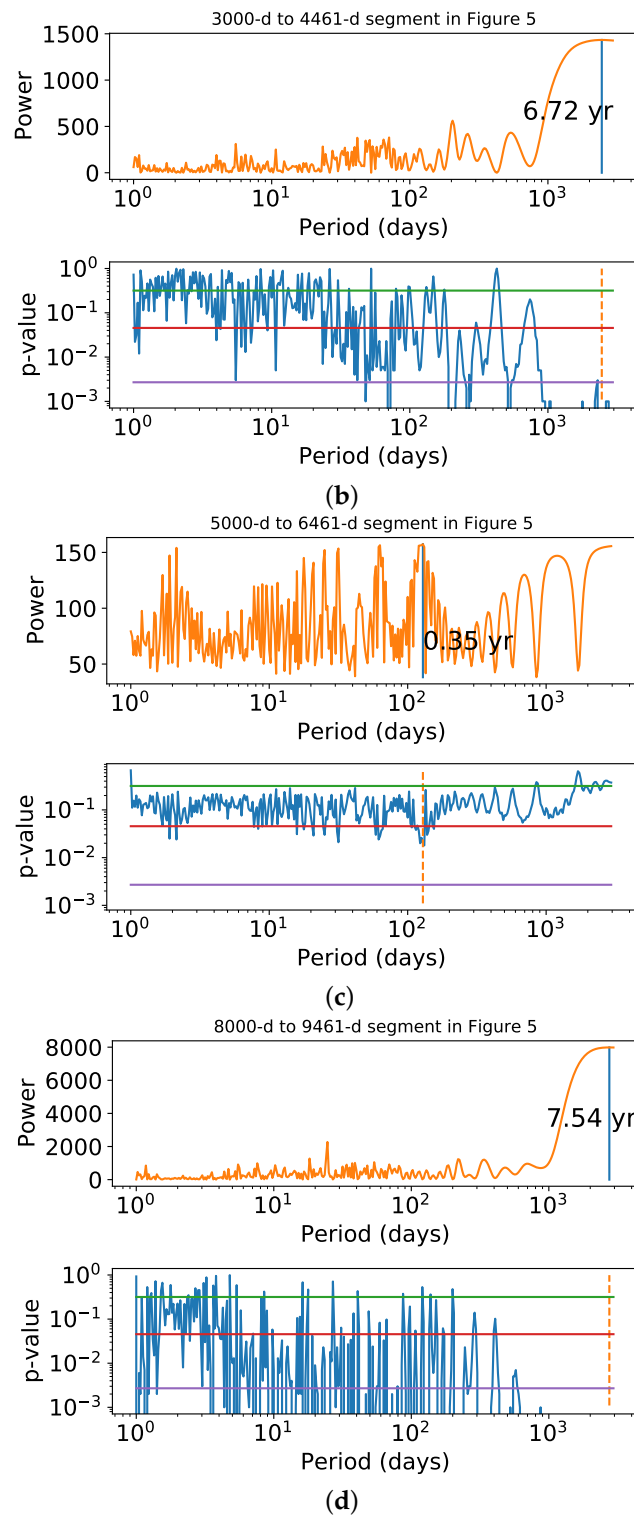
Figure 11. Panel (**a**) is the same in Figure 5. Panel (**b**–**d**) are power and *p*-value diagrams for several 4 years segments selected from Panel (**a**). Similar plots for the total TSI data are shown in Panel (**d**) of Figure 5. The green, red, and purple horizontal lines in Panel (**b**–**d**) show the 1-sigma, 2-sigma, and 3-sigma uncertainty, respectively. The strongest cycles are marked by vertical lines.
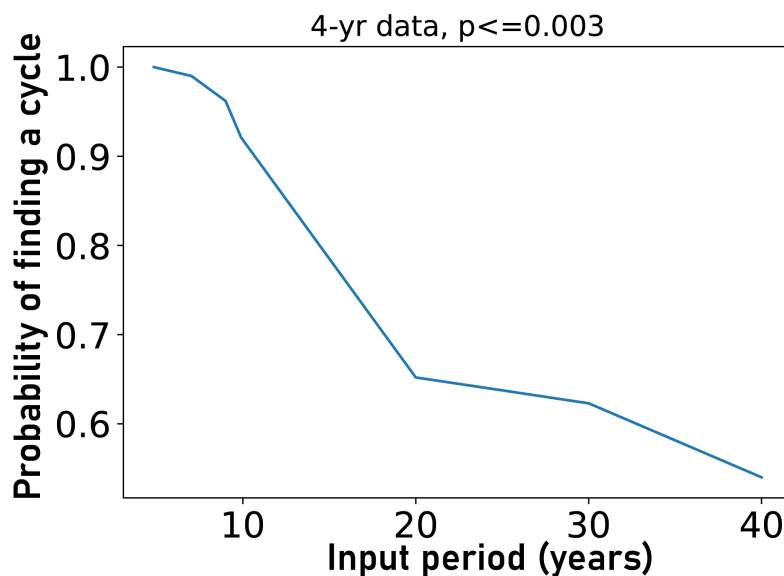
Figure 12. This is the probability to find a magnetic activity cycle using our smoothness metric. As noted in Section 3.1, we accept a signal as a detected cycle when the *p*-value is less than 0.003. We randomly select a 4 years segment from the synthetic light curve and apply our smoothness metric (this length is the same as that which we use when analyzing our sample stars from Kepler). Each input period has 100 tests.

(**a**)

Figure 13. *Cont.*

(**b**)
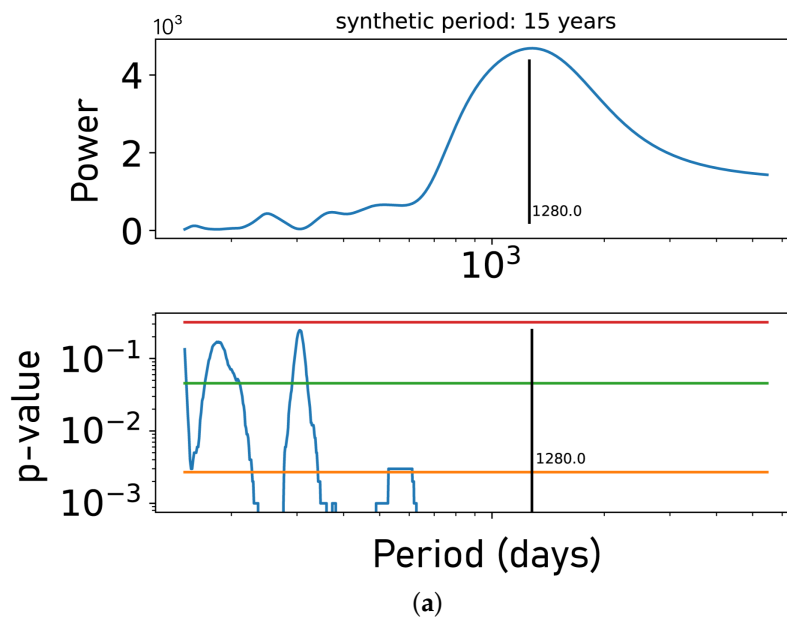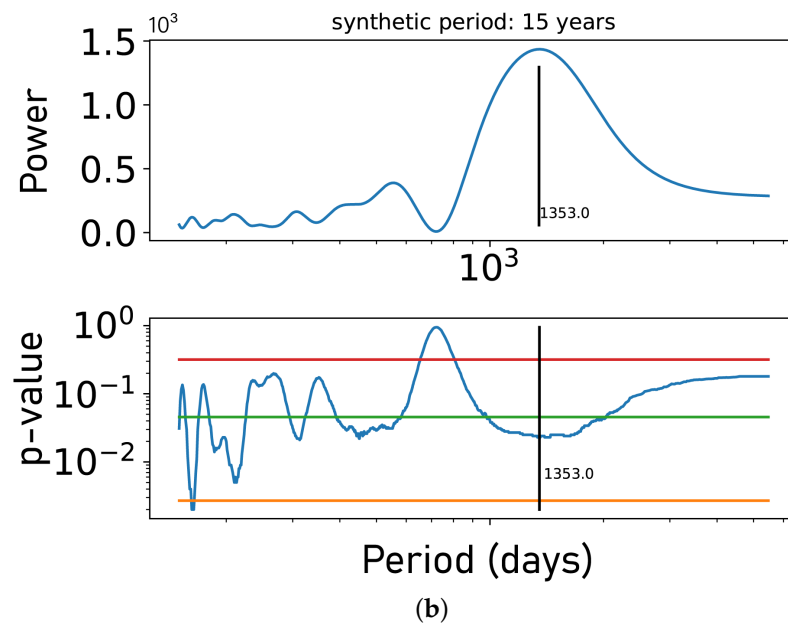
Figure 13. Two examples of the tests are shown in Figure 12. Panel (**a**) is from a single test and panel (**b**) from another. Both tests have a 15 years synthetic period, and an ~4 years segment is used for analysis because the Kepler observation lasts about 4 years. Both tests find a signal at about 1300 days, but the second test does not pass our *p*-value criteria (*p*-value < 3-sigma). The vertical line and corresponding label give the position of the strongest signal; the red, green, and orange horizontal lines show the 1-sigma, 2-sigma, and 3-sigma uncertainties, respectively.

3.3.4. Evolutionary Stages of the Stars with Activity Cycles

Figure 14 shows the distribution of 4455 stars with activity cycle candidates found in this work on the T_{eff} vs. $\log g$ diagrams and divides this distribution with the total distribution to obtain the probability of finding activity cycles for stars with different T_{eff} and $\log g$. T_{eff} and $\log g$ are from Kepler DR25 [55]. It can be found that very high-temperature stars (unstable) and low-temperature giants (deeper convection zone) are more likely to have activity cycles. We also plotted the same distribution of activity cycle candidates found by Reinhold et al. [29] in Figure 15 and found that lower temperature main sequence stars are more likely to have activity cycles (deeper convection zone), but our results do not reflect this at the moment. We then remove stars with cycle periods between 260 and 750 days from our results, since these cycles are more likely to be false signals due to CCD effects (Section 3.3.2), and plot the same diagrams (Figure 16). We find a concentrated distribution of the removed stars (certainly the most dense area of stars in the Kepler sample, since the CCD effect is independent of the properties of the stars), and after removing them, our results also show a similar relation to Figure 15 (but not as pronounced as Reinhold et al. [29]), and the relation in Figure 14 is still retained. Considering that our results contain spurious cycles or possible pulsators, especially at high effective temperature and low surface gravity, the above is a qualitative discussion only and does not constitute any conclusion.
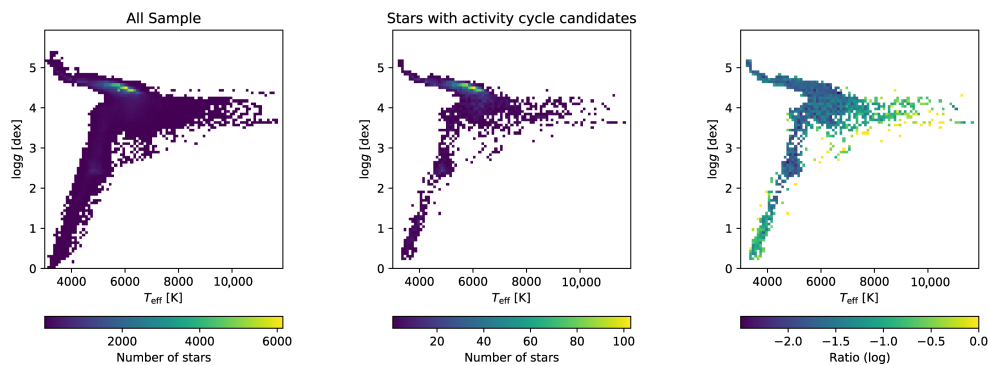
Figure 14. The left panel is the T_{eff} vs. $\log g$ diagram of all Kepler targets. The middle panel is the same diagram of 4455 stars with activity cycle candidates found by this work. The right panel is the ratio of the middle and the left.
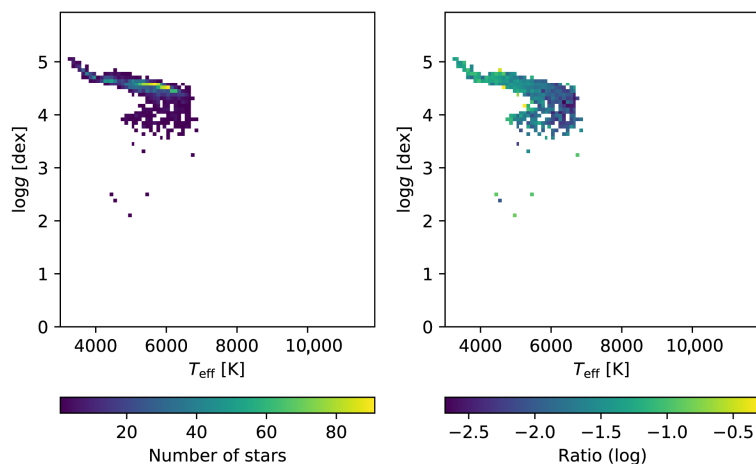
Figure 15. The left panel is the same as the middle panel of Figure 14, and the right panel is the same as the right panel of Figure 14 but using Reinhold et al. [29] cycle candidates.
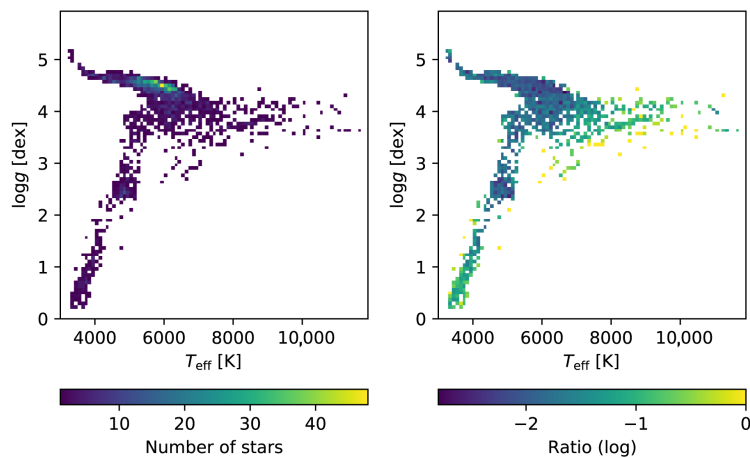
Figure 16. The left panel is the same as the middle panel of Figure 14, and the right panel is the same as the right panel of Figure 14, but remove the stars with cycle candidates between 260 days and 750 days, since these cycles are more likely to be false signals due to CCD effects (Section 3.3.2).

4. Discussion

As mentioned in Section 1, many previous works have studied activity cycles; we make a comparison with our results in Section 4.2. For aperture photometry light curves, many previous works used R_{var} and S_{ph} to analyze activity cycles, a comparison between R_{var}, S_{ph}, and our method is given in Section 4.3. No matter what method we use, the *p*-value is helpful, but the *p*-value is sometimes unreliable, which is discussed in Section 4.4. Some other discussions are given in Section 4.5.

4.1. Cycle sequence

Out of 34,030 Kepler stars with confirmed rotation periods [46], we found 1189 matches with our activity cycle candidates. The plot of the rotation period vs. magnetic activity cycle is given in Figure 17. If only focusing on the bottom portion of Figure 17, it seems to weakly support the possible correlation reported by previous authors [5,51,56–59] between the rotation period and the activity cycle period of a star. As stated in Sections 3.3.2 and 3.3.3, around 20 percent of the detections are false, and 50 percent are likely the lower limits of the real cycle periods, but the periods shorter than 1 year are more reliable, so it is reasonable to focus on Figure 17's bottom portion. If there is no correlation between a star's rotation period and its activity cycle period, stars should show in the bottom right corner, but none do. The odds of this occurring randomly is approximately 2^{-18}. However, we cannot support the cycle sequence with just a few stars that have an activity cycle period of less than 1 year in Figure 17. The cycle sequence is still controversial.
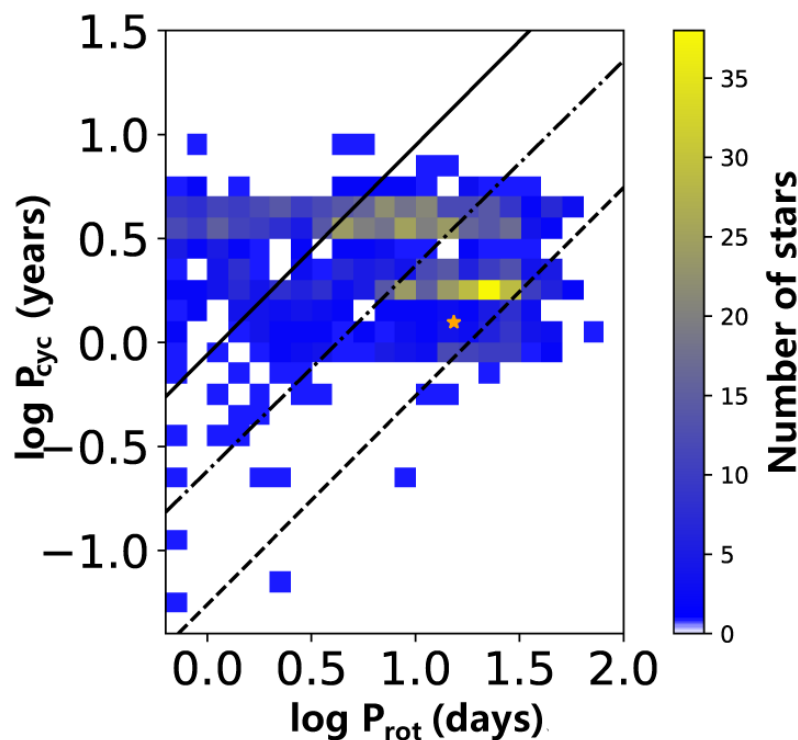
Figure 17. Rotation period P_{rot} vs. magnetic activity cycle period P_{cyc} of 1189 Kepler targets. Note that false cycles remain in our results from applying our smoothness metric. The solid line is the active sequence, the dash-dotted line is the inactive sequence, and the dashed line is the short-cycle sequence as defined by Ferreira Lopes et al. [51]. The color represents the number of stars. The orange star marker is KIC 9017220.

4.2. Comparison with Previous Work

As mentioned in Section 1, there are many stellar phenomena (spots, X-ray emission (flares), p-modes, etc.) which are used to find activity cycles, as these are all found to have an ~11 years cycle on the Sun. In other words, the confirmation of an activity cycle requires multiband and

long-time continuous observation, in principle. From this point of view, there is no other activity cycle as credible as the solar cycle. The most credible cycle till now, except for the Sun, may be the 7.41 years cycle of HD 173701 [54]. In Karoff et al. [54], they use spectroscopic data provided by the Mount Wilson HK project, the Nordic Optical Telescope, and the Keck telescope and aperture photometry data from the Kepler mission; such a rich collection of data is hard to reproduce for other stars. In this work, our smoothness metric classifies HD 173701 as one of our 4455 cycle candidates. Although the 7.41 years cycle is longer than the 4 years observation period of Kepler, based on Section 3.3.3, when analyzing an ∼4 years segment of a light curve with a cycle longer than 4 years, our smoothness metric is still able to detect a cycle (about 99 percent probability of detecting a 7.41 years cycle, as shown in Figure 12). Strictly speaking, if only the Kepler data is used, our smoothness metric can only provide activity cycle candidates, and further observations are needed for confirmation of the magnetic activity cycle. The closest work to our study is Reinhold et al. [29], in which only 23,601 Kepler targets are analyzed and 3203 activity cycle candidates are detected. Our metric is able to be applied to a broader collection of Kepler targets, although we found a small overlap of 114 stars as cycle candidates detected by this work (total of 1189 candidates) and Reinhold et al. [29] (total of 3203 candidates). A brief comparison is given in Figure 18. Montet et al. [27] provide several cycle candidates using Kepler data, and we found four stars detected in common with this work; Han et al. [60] found several beating patterns (which may be related to activity cycles), and we found three stars detected in common with this work. These stars in common are also marked in Figure 18. Some works analyze stars that have been observed for tens of years and they find several tens of activity cycles [5,51,56,61,62], but we found no stars detected in common with this work.

In Figure 18, the distribution of cycle periods from the literature is more uniform, but there are still peaks close to integer years if looking closely. The work in the literature contains fewer data points, so its sampling function is more uniform. The effect of the sampling function exists but is not readily apparent. Very few discussions in the literature detail sampling function effects as thoroughly as we do.
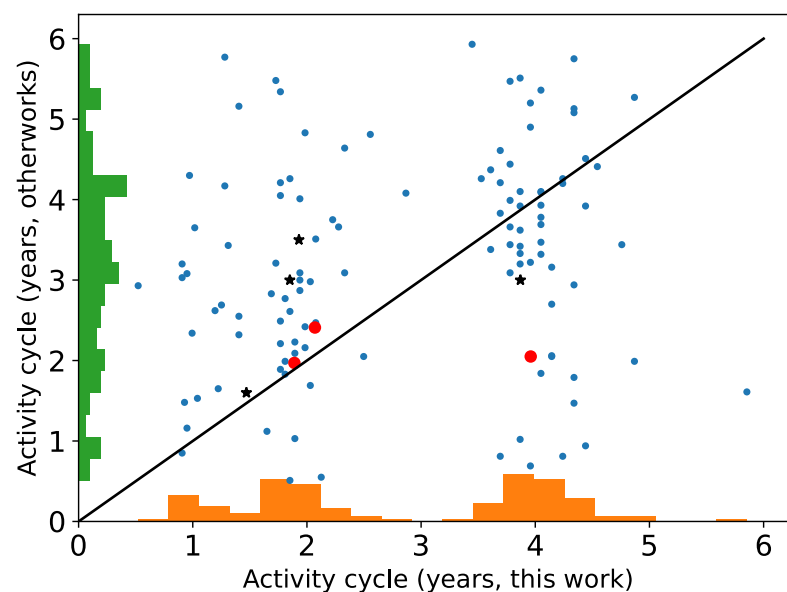
Figure 18. Magnetic activity periods compared for candidate stars detected in this work with stars which have previously been detected by other works. The periods of our commonly detected candidate stars are compared with the results of Reinhold et al. [29] (114 small blue dots), Montet et al. [27] (4 star-like dots), and Han et al. [60] (3 large red dots). Histograms of the periods from this work are along the *x*-axis, and those from Reinhold et al. [29] are along the *y*-axis. The line marks the one-to-one relationship between activity cycles.

4.3. Comparison: R_{var}, S_{ph}, and Our Metric

R_{var}, S_{ph}, and our metric are all suitable for Kepler long-cadence light curves. R_{var} and S_{ph} are insensitive to flares because they neglect outliers. Our metric is sensitive to flares because most flares appear as outliers due to the low time resolution in the Kepler long-cadence light curves. Note that if there are too many flares, R_{var} and S_{ph} would still be affected.

As for spots, if a star has rotational modulation caused by spots, R_{var} and S_{ph} measure the amplitude of the spot modulation, in which case, the segment of R_{var} and S_{ph} must be set longer than the rotation period. The 30 days to 90 days segments are always used when using the R_{var} method, which means 10 to 50 Kepler data points are provided for Fourier transformation. R_{var} and S_{ph} work better on fast rotators in the sense of the number of data points. Because they do not need a long segment of the light curve, they can obtain more data points for fast rotators. Our smoothness metric filters out the rotational modulation and then finds the outliers, allowing us to provide more data points; however, if the star rotates too quickly, the smoothing filter may be invalid and our metric will fail. Our metric works better on slow rotators. For slow rotators, our metric is more likely to find a lower limit of the cycle, but it is still evidence. If using the R_{var} or S_{ph} method, there are insufficient data points to provide evidence. The above is based on the reality that Kepler provides 4 years light curves. If we apply our smoothness metric to light curves of longer time and higher time resolution, the rotation speed does not need to be taken into consideration.

We also used the R_{var} method with a 30 days segment on KIC 9017220 for comparison as shown in Figure 19; both methods give a periodic signal at about 400 days, but the one given by the R_{var} method cannot pass the *p*-value test. The similarities and differences between the two methods require more samples and more detailed analysis.

Figure 19. *Cont.*

(b)
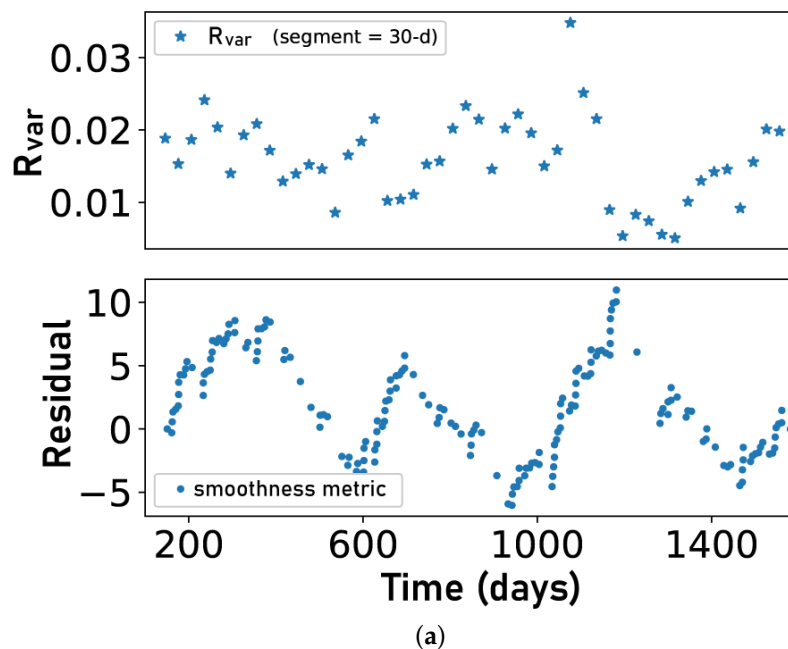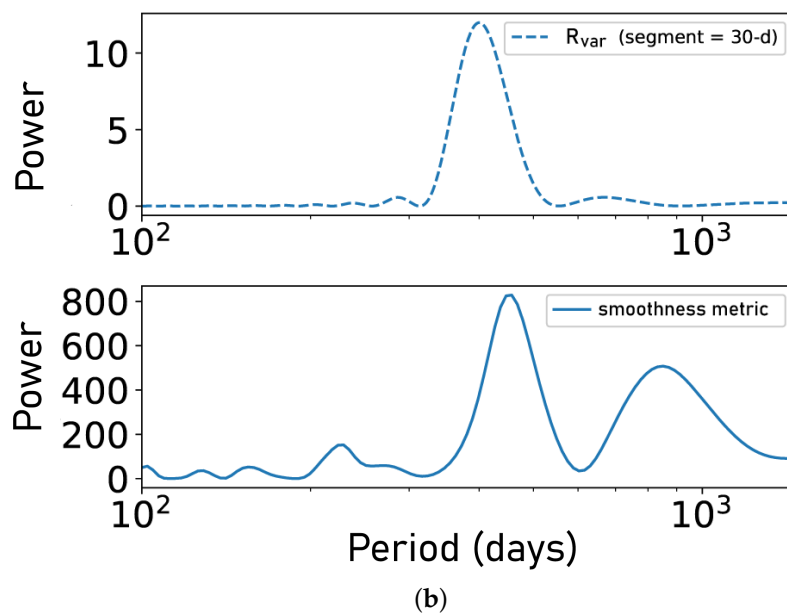
Figure 19. Panel (**a**) is the comparison between the 30 days segment R_{var} of KIC 9017220 and the residuals of outliers as measured using our smoothness metric on KIC 9017220 (same as the right panel of Figure 3). Panel (**b**) is the power spectrum of them (these results are also shown in the left panel of Figure 4). The R_{var} method does not pass our *p*-value test. Our smoothness metric passes our *p*-value test for KIC 9017220, and the *p*-value of our smoothness metric is shown in Figure 4.

4.4. Invalidity of the p-Value Test Caused by a Lack of Data Points

All magnetic activity diagnostics applied to light curves to determine activity cycles involve measuring the time series. In practice, the time series is not continuous but consists of a series of data points. If the data points of the time series do not have the same interval, some special methods are needed to apply Fourier transformation, such as Lomb–Scargle, which is used in this work. For Lomb–Scargle, *p*-value can be obtained through strict mathematical steps, but it only represents the FAP of this step. To obtain the overall FAP, all steps need to be simulated by the Monte Carlo method. No matter how the Monte Carlo simulation is designed, it involves a time series composed of the data points. We show below that when there are not enough data points, the overall FAP given by Monte Carlo simulation is invalidated when the real data contains high-frequency periods. The existence of high-frequency periods invalidates the results by inducing a leakage effect (as we define below), and we are thus unable to measure an accurate probability distribution.

To test the effects due to high frequencies, we consider the R_{var} method as used by Reinhold et al. [29]. In their work, they use $\sim$14 time-series data points and the Lomb–Scargle periodogram to measure R_{var}. The low number of points along the light curve is chosen because when using the R_{var} method the length of the segments (one segment can give one data point) cannot be too close to the rotation period. Adopting $\sim$14 data points every 4 years is sufficient to distinguish the signal between 0.5 years and 6 years, but it cannot prevent the leakage effect from a higher frequency. To understand the leakage effect more clearly, we conduct a Monte Carlo simulation. Firstly, we set a period randomly that is shorter than 0.5 years. Secondly, we generate several data points with equal time intervals. These points follow a sine curve with the same period. Thirdly, we find how many times the highest peak between 0.5 years and 6 years has a *p*-value less than 0.05 using Fourier transformation. We define the leakage effect as the incorrect detection of a 0.5–6 years cycle when the true cycle is shorter than 0.5 years. The occurrence probability of leakage events is taken as the dependent variable, and the number of data points is taken as the independent variable. The *p*-value is calculated in the same manner as Reinhold et al. [29]. The result is depicted in Figure 20. It is clear that the more data points we use, the smaller the probability we find of detecting a false signal that can pass the *p*-value test. It should be mentioned that

this does not mean almost 50 percent of cycles found by Reinhold et al. [29] are false signals. We cannot use this simulation result as a supplement to the *p*-value because an unknown parameter is needed: the probability of the existence of a high-frequency signal. That is why we think this result indicates the limitation of the *p*-value. This is consistent with the claim of Wasserstein et al. [63], such that we cannot believe a conclusion just because the FAP reaches the standard. The only thing we can do is to obtain more data.
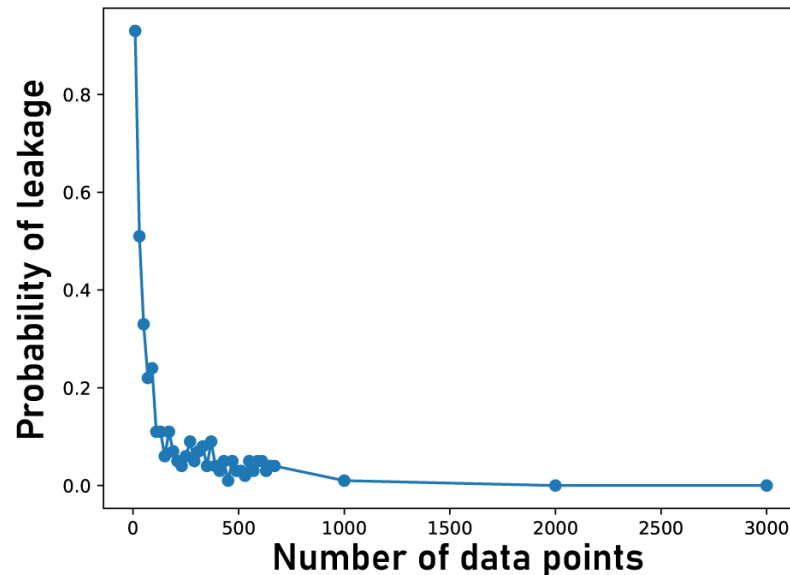
Figure 20. Mock stellar light curve test results for the leakage effect. Along the *x*-axis is the number of data points provided to Fourier transformation. The data points have equal time intervals with a total length of 4 years, distributed as a sine function. The period of the sine function is shorter than 0.5 years. The *y*-axis is the probability of finding a signal between 0.5 and 6 years that passes the *p*-value test.

4.5. Other Discussions

As mentioned before, we need to generate synthetic light curves with changing magnetic activity. Aigrain et al. [53] have considered this same case. A simple method based on the relationship between the smoothness of the light curve and magnetic activity is provided for reference only. We set a sine function, then add Gaussian noise to the sine function, making sure the sigma value is adjustable at different times. The sigma value of Gaussian noise is related to the smoothness of the synthetic light curve in this case. The specific distribution of sigma should be set, which refers to the properties of the real light curves.

We may miss detecting a cycle due to Kepler's Presearch Data Conditioning software used for pre-processing [64]. Different from our metric to detect outliers, Kepler's Transiting Planet Search pipeline module returns a Threshold Crossing Event which is used for detecting planets. In order to minimize false planet detection by the pipeline, Twicken et al. [64] seeks to remove outliers as part of the Pre-search Data Conditioning software. Some of the removed outliers are false data points. Some of them are real data points (but not planets) and can thus cause a false planet detection by Kepler's Transiting Planet Search pipeline module. If too many real outliers are removed, it may affect our smoothing metric method.

The number of outliers per unit time given by our method can be used to estimate the strength of magnetic activity, but we do not recommend using this to compare the strength of magnetic activity of different stars because some stars may be quiet most of the time and strongly active for a short time, but the number of outliers is small. The deviation of outliers may be more appropriate to estimate the strength, but as we mentioned, the deviation of outliers has a large error, and our method only focuses on the number of outliers in

order to avoid this error. For the type of stars just mentioned, the number of outliers does not truly reflect the intensity of their activity relative to other types of stars. By using the histograms of the outliers of two stars (Figure 21), we roughly detect the asymmetry of the cycles. Currently, our method cannot detect the Waldmeier effect [65] because the number of outliers is not a good quantitative description of the amplitude of a cycle, as mentioned earlier in this paragraph. More work is needed to robustly locate the peak and amplitude of cycles using our smoothness metric.
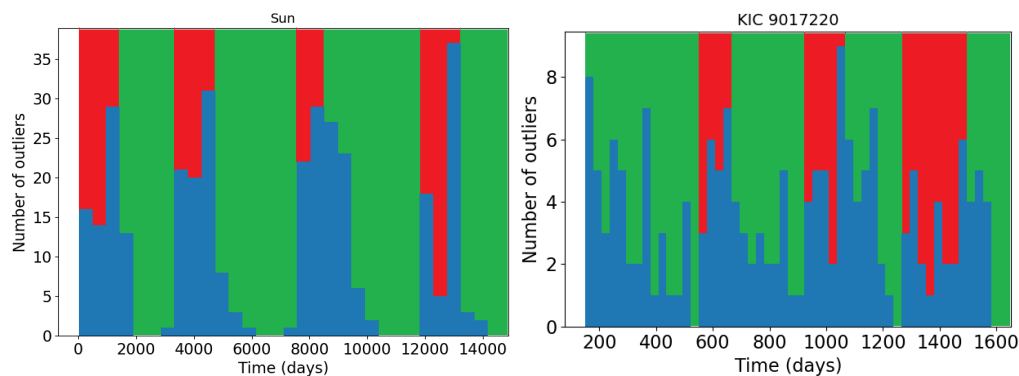
Figure 21. The blue bars are the histogram of outliers of the Sun and KIC 9017220. The red background roughly marks the interval where magnetic activity becomes stronger, and the green marks the interval where it declines, roughly.

Based on the issues discussed above, several investigations remain to be conducted in the near future. Firstly, we can compare the phases of the "solar cycle" and the "smoothness cycle" in detail to understand how well they synchronize. We can perform a similar test on other stars to check whether the synchronization is a coincidence or not. If the synchronization is not a coincidence, the physical mechanism behind it requires further interpretation. Secondly, the method adopted in this work can be used on other light-curve data in the near future. Thirdly, we could combine spectral data with our work. For example, the Large sky Area Multi-Object fibre Spectroscopic Telescope (LAMOST [66–69]) survey data has duplicate observation targets with Kepler. The LAMOST spectrum can be used to analyze stellar activity [70,71], although the main goal of the LAMOST survey is the exploration of the formation and evolution of the Galaxy [72–74]. Fourthly, we can compare the results of our smoothness metric to other stars that have confirmed activity cycles, such as Section 3.2, where we confirmed the 11 years magnetic activity cycle of the Sun using our metric. We considered HD 173701 because it has a confirmed activity cycle and has been observed by Kepler; however, the cycle of HD 173701 is too long (7.41 years [54]), so more work is required to find appropriate targets. Fifthly, our method may be helpful to study the asymmetry of the cycles and the Waldmeier Effect [65]. If a large number of activity cycles can be found, the most useful prospect of our study will be to perform a statistical analysis, which may be helpful for future studies on the origin of activity cycles.

5. Conclusions

In this work, we define the smoothness metric, which we apply to stellar light curves in order to detect smoothness cycles that correlate with stellar magnetic activity cycles. The uniqueness of our metric is that it uses the outliers from the light curves in order to measure the smoothness cycles. We apply our metric to Kepler long-cadence light curves and detect 4455 smoothness cycles, which correlates to finding 4455 stellar magnetic activity cycle candidates. False cycles are contained in the cycle candidates we found. We analyzed the causes of false cycles in detail. We test our method using the total solar irradiance (TSI [42]) data and measure an 11 years smoothness cycle. This demonstrates that there is a relationship between the smoothness of the light curve and the magnetic activity of the star. We use the number of outliers to characterize smoothness in order to collect

a large number of stars with activity cycles from Kepler long-cadence light curves. We select several samples as a preliminary test of our method using Kepler data. We find that light curves with moderate variation are most appropriate for our metric because they are easy to smooth. The R_{var} method and our method are complementary to each other. Our smoothness metric is able to detect the relatively more credible ∼457 days activity cycle of KIC 9017220. We make note of several weaknesses which we find when applying both methods to the Kepler targets. Some slow rotators are not applicable to the R_{var} method due to the the 4 years limitation of Kepler data. A strength of our smoothness metric is its applicability to a large number and broad range of light curves, which thus allows us to detect a large number of magnetic activity cycle candidates. By using our method on 92,084 Kepler targets with 17 or 16 quarters, we find several causes which produce false signals. The difference between Kepler CCD channels can introduce false signals. Decreasing the sampling frequency can solve this problem, but in turn increases the likelihood of the leakage effect and invalidates the *p*-value test. When periods longer than Kepler's 4 years light curves exist, we measure the probability of detecting a periodic signal using our smoothness metric, finding that this probability of detecting a period decreases as the length of the period increases. With the minimization of false detections in future work, we will be able to collect a large number of activity cycles, which will be a prime sample for statistical analysis.

Author Contributions: Conceptualization, G.Z. and Y.-F.S.; methodology, Y.-F.S.; software, Y.-F.S.; validation, Y.-F.S., G.Z. and S.A.B.; formal analysis, Y.-F.S.; investigation, Y.-F.S.; resources, G.Z.; data curation, Y.-F.S.; writing—original draft preparation, Y.-F.S.; writing—review and editing, G.Z. and S.A.B.; visualization, Y.-F.S., G.Z. and S.A.B.; supervision, G.Z.; project administration, G.Z.; funding acquisition, G.Z. All authors have read and agreed to the published version of the manuscript.

Data Availability Statement: The data presented in this study are available on request from the first author. The data are not publicly available due to the false cycle periods in the results, which may be misused by readers who have not read the literature carefully.

Conflicts of Interest: The authors declare no conflict of interest.

References

1. Svensmark, H.; Friis-Christensen, E. Variation of cosmic ray flux and global cloud coverage-a missing link in solar-climate relationships. *J. Atmos.-Sol.-Terr. Phys.* **1997**, *59*, 1225–1232. [CrossRef]
2. Charvàtovà, I. Solar-Terrestrial and Climatic Phenomena in Relation to Solar Inertial Motion. *Surv. Geophys.* **1997**, *18*, 131–146. [CrossRef]
3. Kane, S.R.; Thirumalachari, B.; Henry, G.W.; Hinkel, N.R.; Jensen, E.L.N.; Boyajian, T.S.; Fischer, D.A.; Howard, A.W.; Isaacson, H.T.; Wright, J.T. Stellar Activity and Exclusion of the Outer Planet in the HD 99492 System. *Astrophys. J. Lett.* **2016**, *820*, L5. [CrossRef]
4. Saar, S.H.; Brandenburg, A. Time Evolution of the Magnetic Activity Cycle Period. II. Results for an Expanded Stellar Sample. *Astrophys. J.* **1999**, *524*, 295–310. [CrossRef]
5. Böhm-Vitense, E. Chromospheric Activity in G and K Main-Sequence Stars, and What It Tells Us about Stellar Dynamos. *Astrophys. J.* **2007**, *657*, 486–493. [CrossRef]
6. Charbonneau, P. Dynamo Models of the Solar Cycle. In *Solar and Stellar Dynamos, Saas-Fee Advanced Courses*; Springer: Berlin/Heidelberg, Germany, 2013; Volume 39, p. 87; ISBN 978-3-642-32092-7. [CrossRef]
7. Morris, B.M.; Hebb, L.; Davenport, J.R.A.; Rohn, G.; Hawley, S.L. The Starspots of HAT-P-11: Evidence for a Solar-like Dynamo. *Astrophys. J.* **2017**, *846*, 99. [CrossRef]
8. Valio, A.; Estrela, R.; Netto, Y.; Bravo, J.P.; de Medeiros, J.R. Activity and Rotation of Kepler-17. *Astrophys. J.* **2017**, *835*, 294. [CrossRef]
9. Mathur, S.; García, R.A.; Ballot, J.; Ceillier, T.; Salabert, D.; Metcalfe, T.S.; Régulo, C.; Jiménez, A.; Bloemen, S. Investigating magnetic activity of F stars with the Kepler mission. In *IAU Symposium*; Petit, P.; Jardine, M.; Spruit, H.C., Eds.; Magnetic Fields throughout Stellar Evolution; Cambridge University Press: Cambridge, UK, 2014; Volume 302, pp. 222–223. [CrossRef]

10. Basri, G.; Walkowicz, L.M.; Batalha, N.; Gilliland, R.L.; Jenkins, J.; Borucki, W.J.; Koch, D.; Caldwell, D.; Dupree, A.K.; Latham, D.W.; et al. Photometric Variability in Kepler Target Stars. II. An Overview of Amplitude, Periodicity, and Rotation in First Quarter Data. *Astrophys. J.* **2011**, *141*, 20. [CrossRef]

11. Sanz-Forcada, J.; Stelzer, B.; Metcalfe, T.S. *ι*Horologi, the first coronal activity cycle in a young solar-like star. *Astron. Astrophys.* **2013**, *553*, L6. [CrossRef]

12. Woodard, M.F.; Noyes, R.W. Change of solar oscillation eigenfrequencies with the solar cycle. *Nature* **1985**, *318*, 449–450. doi: [CrossRef]

13. Libbrecht, K.G.; Woodard, M.F. Solar-cycle effects on solar oscillation frequencies. *Nature* **1990**, *345*, 779–782. [CrossRef]

14. Jimenez-Reyes, S.J.; Regulo, C.; Palle, P.L.; Roca Cortes, T. Solar activity cycle frequency shifts of low-degree p-modes. *Astron. Astrophys.* **1998**, *329*, 1119–1124.

15. García, R.A.; Mathur, S.; Salabert, D.; Ballot, J.; Régulo, C.; Metcalfe, T.S.; Baglin, A. CoRoT Reveals a Magnetic Activity Cycle in a Sun-Like Star. *Science* **2010**, *329*, 1032. [CrossRef] [PubMed]

16. Salabert, D.; Régulo, C.; Pérez Hernández, F.; García, R.A. Frequency dependence of p-mode frequency shifts induced by magnetic activity in Kepler solar-like stars. *Astron. Astrophys.* **2018**, *611*, A84. [CrossRef]

17. Kiefer, R.; Schad, A.; Davies, G.; Roth, M. Stellar magnetic activity and variability of oscillation parameters: An investigation of 24 solar-like stars observed by Kepler. *Astron. Astrophys.* **2017**, *598*, A77. [CrossRef]

18. Metcalfe, T.S.; Monteiro, M.J.P.F.G.; Thompson, M.J.; Chaplin, W.J.; Basu, S.; Bonanno, A.; Di Mauro, M.P.; Doğan, G.; Eggenberger, P.; Karoff, C.; et al. Asteroseismology of solar-type stars with Kepler: II. Stellar modeling. *Astron. Nachrichten* **2010**, *331*, 977. [CrossRef]

19. Mathur, S.; Bruntt, H.; Catala, C.; Benomar, O.; Davies, G.R.; García, R.A.; Salabert, D.; Ballot, J.; Mosser, B.; Régulo, C.; et al. Study of HD 169392A observed by CoRoT and HARPS. *Astron. Astrophys.* **2013**, *549*, A12. [CrossRef]

20. Santos, A.R.G.; Campante, T.L.; Chaplin, W.J.; Cunha, M.S.; Lund, M.N.; Kiefer, R.; Salabert, D.; García, R.A.; Davies, G.R.; Elsworth, Y.; et al. Signatures of Magnetic Activity in the Seismic Data of Solar-type Stars Observed by Kepler. *Astrophys. J.* **2018**, *237*, 17. [CrossRef]

21. Santos, A.R.G.; Campante, T.L.; Chaplin, W.J.; Cunha, M.S.; van Saders, J.L.; Karoff, C.; Metcalfe, T.S.; Mathur, S.; García, R.A.; Lund, M.N.; et al. Signatures of Magnetic Activity: On the Relation between Stellar Properties and p-mode Frequency Variations. *Astrophys. J.* **2019**, *883*, 65. [CrossRef]

22. Baliunas, S.L.; Donahue, R.A.; Soon, W.H.; Horne, J.H.; Frazer, J.; Woodard-Eklund, L.; Bradford, M.; Rao, L.M.; Wilson, O.C.; Zhang, Q.; et al. Chromospheric variations in main-sequence stars. *Astrophys. J.* **1995**, *438*, 269–287. [CrossRef]

23. Baliunas, S.L. Stellar Activity Cycles. Cool Stars, Stellar Systems and the Sun. In *Lecture Notes in Physics*; Zeilik, M., Gibson, D.M., Eds.; Springer: Berlin, Germany, 1986; Volume 254, p. 3.

24. Hall, J.C.; Lockwood, G.W.; Skiff, B.A. The Activity and Variability of the Sun and Sun-like Stars. I. Synoptic Ca II H and K Observations. *Astrophys. J.* **2007**, *133*, 862–881. [CrossRef]

25. Lockwood, G.W.; Hall, J.C.; Skiff, B.A.; Henry, G.W.; Radick, R.R.; Baliunas, S.L.; Soon, W.; Donahue, R.A. Gauging the Sun: Comparative photometric and magnetic activity measurements of sunlike stars, 1984-2001. American Astronomical Society Meeting Abstracts #200. *Bull. Am. Astron. Soc.* **2002**, *34*, 651.

26. Oláh, K.; Kolláth, Z.; Granzer, T.; Strassmeier, K.G.; Lanza, A.F.; Järvinen, S.; Korhonen, H.; Baliunas, S.L.; Soon, W.; Messina, S.; et al. Multiple and changing cycles of active stars. II. Results. *Astron. Astrophys.* **2009**, *501*, 703–713. [CrossRef]

27. Montet, B.T.; Tovar, G.; Foreman-Mackey, D. Long-term Photometric Variability in Kepler Full-frame Images: Magnetic Cycles of Sun-like Stars. *Astrophys. J.* **2017**, *851*, 116. [CrossRef]

28. Morgenthaler, A.; Petit, P.; Morin, J.; Aurière, M.; Dintrans, B.; Konstantinova-Antova, R.; Marsden, S. Direct observation of magnetic cycles in Sun-like stars. *Astron. Nachrichten* **2011**, *332*, 866. [CrossRef]

29. Reinhold, T.; Cameron, R.H.; Gizon, L. Evidence for photometric activity cycles in 3203 Kepler stars. *Astron. Astrophys.* **2017**, *603*, A52. [CrossRef]

30. Basri, G.; Walkowicz, L.M.; Reiners, A. Comparison of Kepler Photometric Variability with the Sun on Different Timescales. *Astrophys. J.* **2013**, *769*, 37. [CrossRef]

31. Mathur, S.; García, R.A.; Ballot, J.; Ceillier, T.; Salabert, D.; Metcalfe, T.S.; Régulo, C.; Jiménez, A.; Bloemen, S. Magnetic activity of F stars observed by Kepler. *Astron. Astrophys.* **2014**, *562*, A124. [CrossRef]

32. Salabert, D.; García, R.A.; Beck, P.G.; Egeland, R.; Pallé, P.L.; Mathur, S.; Metcalfe, T.S.; do Nascimento, J.D.J.; Ceillier, T.; Andersen, M.F.; et al. Photospheric and chromospheric magnetic activity of seismic solar analogs. Observational inputs on the solar-stellar connection from Kepler and Hermes. *Astron. Astrophys.* **2016**, *596*, A31. [CrossRef]

33. Salabert, D.; García, R.A.; Jiménez, A.; Bertello, L.; Corsaro, E.; Pallé, P.L. Photospheric activity of the Sun with VIRGO and GOLF. Comparison with standard activity proxies. *Astron. Astrophys.* **2017**, *608*, A87. [CrossRef]

34. Reinhold, T.; Shapiro, A.I.; Solanki, S.K.; Montet, B.T.; Krivova, N.A.; Cameron, R.H.; Amazo-Gómez, E.M. The Sun is less active than other solar-like stars. *Science* **2020**, *368*, 518–521. [CrossRef] [PubMed]

35. García, R.A.; Ceillier, T.; Salabert, D.; Mathur, S.; van Saders, J.L.; Pinsonneault, M.; Ballot, J.; Beck, P.G.; Bloemen, S.; Campante, T.L.; et al. Rotation and magnetism of Kepler pulsating solar-like stars. Towards asteroseismically calibrated age-rotation relations. *Astron. Astrophys.* **2014**, *572*, A34. [CrossRef]

36. Estrela, R.; Valio, A. Stellar Magnetic Cycles in the Solar-like Stars Kepler-17 and Kepler-63. *Astrophys. J.* **2016**, *831*, 57. [CrossRef]

37. Notsu, Y.; Maehara, H.; Shibayama, T.; Honda, S.; Notsu, S.; Namekata, K.; Nogami, D.; Shibata, K. Statistical Properties of Superflares on Solar-Type Stars with Kepler Data. In Proceedings of the 19th Cambridge Workshop on Cool Stars, Stellar Systems, and the Sun (CS19), Uppsala, Sweden, 6–10 June 2016; p. 119. [CrossRef]
38. Davenport, J.R.A. The Kepler Catalog of Stellar Flares. *Astrophys. J.* **2016**, *829*, 23. [CrossRef]
39. Bastien, F.A.; Stassun, K.G.; Basri, G.; Pepper, J. An observational correlation between stellar brightness variations and surface gravity. *Nature* **2013**, *500*, 427–430. [CrossRef] [PubMed]
40. Chaplin, W.J.; Bedding, T.R.; Bonanno, A.; Broomhall, A.M.; García, R.A.; Hekker, S.; Huber, D.; Verner, G.A.; Basu, S.; Elsworth, Y.; et al. Evidence for the Impact of Stellar Activity on the Detectability of Solar-like Oscillations Observed by Kepler. *Astrophys. J. Lett.* **2011**, *732*, L5. [CrossRef]
41. He, H.; Wang, H.; Yun, D. Activity Analyses for Solar-type Stars Observed with Kepler. I. Proxies of Magnetic Activity. *Astrophys. J. Suppl. Ser.* **2015**, *221*, 18. [CrossRef]
42. Domingo, V.; Ermolli, I.; Fox, P.; Fröhlich, C.; Haberreiter, M.; Krivova, N.; Kopp, G.; Schmutz, W.; Solanki, S.K.; Spruit, H.C.; et al. Solar Surface Magnetism and Irradiance on Time Scales from Days to the 11-Year Cycle. *Space Sci. Rev.* **2009**, *145*, 337–380. [CrossRef]
43. Batalha, N.M.; Borucki, W.J.; Koch, D.G.; Brown, T.M.; Caldwell, D.A.; Latham, D.W. Characteristics of the Kepler target stars. *Highlights Astron.* **2010**, *15*, 712–713. [CrossRef]
44. Thompson, S.E.; Caldwell, D.A.; Jenkins, J.M.; Barclay, T.; Barentsen, G.; Bryson, S.T.; Burke, C.J.; Campbell, J.; Catanzarite, J.; Christiansen, J.L.; et al. Kepler Data Release 25 Notes. Available online: https://archive.stsci.edu/kepler/release_notes/release_notes25/KSCI-19065-002DRN25.pdf (accessed on 11 July 2022)
45. Abdul-Masih, M.; Prša, A.; Conroy, K.; Bloemen, S.; Boyajian, T.; Doyle, L.R.; Johnston, C.; Kostov, V.; Latham, D.W.; Matijevič, G.; et al. Kepler Eclipsing Binary Stars. VIII. Identification of False Positive Eclipsing Binaries and Re-extraction of New Light Curves. *Astrophys. J.* **2016**, *151*, 101. [CrossRef]
46. McQuillan, A.; Mazeh, T.; Aigrain, S. Rotation Periods of 34,030 Kepler Main-sequence Stars: The Full Autocorrelation Sample. *Astrophys. J. Suppl. Ser.* **2014**, *211*, 24. [CrossRef]
47. Jose, P.D. Sun's motion and sunspots. *Astrophys. J.* **1965**, *70*, 193. [CrossRef]
48. Wolff, C.L.; Patrone, P.N. A New Way that Planets Can Affect the Sun. *Sol. Phys.* **2010**, *266*, 227–246. [CrossRef]
49. Abreu, J.A.; Beer, J.; Ferriz-Mas, A.; McCracken, K.G.; Steinhilber, F. Is there a planetary influence on solar activity? *Astron. Astrophys.* **2012**, *548*, A88. [CrossRef]
50. Stefani, F.; Giesecke, A.; Weber, N.; Weier, T. Synchronized Helicity Oscillations: A Link Between Planetary Tides and the Solar Cycle? *Sol. Phys.* **2016**, *291*, 2197–2212. [CrossRef]
51. Ferreira Lopes, C.E.; Leão, I.C.; de Freitas, D.B.; Canto Martins, B.L.; Catelan, M.; De Medeiros, J.R. Stellar cycles from photometric data: CoRoT stars. *Astron. Astrophys.* **2015**, *583*, A134. [CrossRef]
52. Zhang, X.J.; Deng, L.H.; Fei, Y.; Li, C.; Tian, X.A.; Wan, Z.J. Hemispheric asymmetry of long-term sunspot activity: sunspot relative numbers for 1939–2019. *Mon. Not. R. Astron. Soc.* **2022**, *514*, 1140–1147. [CrossRef]
53. Aigrain, S.; Llama, J.; Ceillier, T.; Chagas, M.L.d.; Davenport, J.R.A.; García, R.A.; Hay, K.L.; Lanza, A.F.; McQuillan, A.; Mazeh, T.; et al. Testing the recovery of stellar rotation signals from Kepler light curves using a blind hare-and-hounds exercise. *Mon. Not. R. Astron. Soc.* **2015**, *450*, 3211–3226. [CrossRef]
54. Karoff, C.; Metcalfe, T.S.; Santos, Â.R.G.; Montet, B.T.; Isaacson, H.; Witzke, V.; Shapiro, A.I.; Mathur, S.; Davies, G.R.; Lund, M.N.; et al. The Influence of Metallicity on Stellar Differential Rotation and Magnetic Activity. *Astrophys. J.* **2018**, *852*, 46. [CrossRef]
55. Mathur, S.; Huber, D. Kepler Stellar Properties Catalog Update for Q1-Q17 DR25 Transit Search. Available online: https://exoplanetarchive.ipac.caltech.edu/docs/KSCI-19097-004.pdf (accessed on 11 July 2022) .
56. Noyes, R.W.; Weiss, N.O.; Vaughan, A.H. The relation between stellar rotation rate and activity cycle periods. *Astrophys. J.* **1984**, *287*, 769–773. [CrossRef]
57. Baliunas, S.L.; Nesme-Ribes, E.; Sokoloff, D.; Soon, W.H. A Dynamo Interpretation of Stellar Activity Cycles. *Astrophys. J.* **1996**, *460*, 848. [CrossRef]
58. Boro Saikia, S.; Marvin, C.J.; Jeffers, S.V.; Reiners, A.; Cameron, R.; Marsden, S.C.; Petit, P.; Warnecke, J.; Yadav, A.P. Chromospheric activity catalogue of 4454 cool stars. Questioning the active branch of stellar activity cycles. *Astron. Astrophys.* **2018**, *616*, A108. [CrossRef]
59. Karak, B.B.; Tomar, A.; Vashishth, V. Stellar dynamos with solar and antisolar differential rotations: Implications to magnetic cycles of slowly rotating stars. *Mon. Not. R. Astron. Soc.* **2020**, *491*, 3155–3164. [CrossRef]
60. Han, H.G.; Cui, K.M.; Liu, J.F.; Yang, H.Q.; Fang, X.; Zhao, R.N. Stellar activity cycles as revealed by long-term beat-like patterns from light curves of Kepler. *Res. Astron. Astrophys.* **2021**, *21*, 142. [CrossRef]
61. Lehtinen, J.; Jetsu, L.; Hackman, T.; Kajatkari, P.; Henry, G.W. Activity trends in young solar-type stars. *Astron. Astrophys.* **2016**, *588*, A38. [CrossRef]
62. Olspert, N.; Lehtinen, J.J.; Käpylä, M.J.; Pelt, J.; Grigorievskiy, A. Estimating activity cycles with probabilistic methods. II. The Mount Wilson Ca H&K data. *Astron. Astrophys.* **2018**, *619*, A6. [CrossRef]
63. Wasserstein, R.L.; Schirm, A.L.; Lazar, N.A. Moving to a World Beyond "p < 0.05". *Am. Stat.* **2019**, *73*, 1–19.

64. Twicken, J.D.; Chandrasekaran, H.; Jenkins, J.M.; Gunter, J.P.; Girouard, F.; Klaus, T.C. Presearch data conditioning in the Kepler Science Operations Center pipeline. In *Software and Cyberinfrastructure for Astronomy, Proceedings of the SPIE Astronomical Telescopes + Instrumentation, San Diego, CA, USA, 27 June–2 July 2010*; Radziwill, N.M., Bridger, A., Eds.; Society of Photo-Optical Instrumentation Engineers (SPIE) Conference Series; SPIE: Bellingham, WA, USA, 2010; Volume 7740, p. 77401U. [CrossRef]
65. Garg, S.; Karak, B.B.; Egeland, R.; Soon, W.; Baliunas, S. Waldmeier Effect in Stellar Cycles. *Astrophys. J.* **2019**, *886*, 132. [CrossRef]
66. Zhao, G.; Chen, Y.Q.; Shi, J.R.; Liang, Y.C.; Hou, J.L.; Chen, L.; Zhang, H.W.; Li, A.G. Stellar Abundance and Galactic Chemical Evolution through LAMOST Spectroscopic Survey. *Chin. J. Astron. Astrophys.* **2006**, *6*, 265–280. [CrossRef]
67. Zhao, G.; Zhao, Y.H.; Chu, Y.Q.; Jing, Y.P.; Deng, L.C. LAMOST spectral survey — An overview. *Res. Astron. Astrophys.* **2012**, *12*, 723–734. [CrossRef]
68. Cui, X.Q.; Zhao, Y.H.; Chu, Y.Q.; Li, G.P.; Li, Q.; Zhang, L.P.; Su, H.J.; Yao, Z.Q.; Wang, Y.N.; Xing, X.Z.; et al. The Large Sky Area Multi-Object Fiber Spectroscopic Telescope (LAMOST). *Res. Astron. Astrophys.* **2012**, *12*, 1197–1242. [CrossRef]
69. Deng, L.C.; Newberg, H.J.; Liu, C.; Carlin, J.L.; Beers, T.C.; Chen, L.; Chen, Y.Q.; Christlieb, N.; Grillmair, C.J.; Guhathakurta, P.; et al. LAMOST Experiment for Galactic Understanding and Exploration (LEGUE) — The survey's science plan. *Res. Astron. Astrophys.* **2012**, *12*, 735–754. [CrossRef]
70. Fang, X.S.; Zhao, G.; Zhao, J.K.; Chen, Y.Q.; Bharat Kumar, Y. Stellar activity with LAMOST - I. Spot configuration in Pleiades. *Mon. Not. R. Astron. Soc.* **2016**, *463*, 2494–2512. [CrossRef]
71. Fang, X.S.; Zhao, G.; Zhao, J.K.; Bharat Kumar, Y. Stellar activity with LAMOST - II. Chromospheric activity in open clusters. *Mon. Not. R. Astron. Soc.* **2018**, *476*, 908–926. [CrossRef]
72. Liu, X.W.; Zhao, G.; Hou, J.L. Preface: The LAMOST Galactic surveys and early results. *Res. Astron. Astrophys.* **2015**, *15*, 1089. [CrossRef]
73. Li, H.N.; Zhao, G.; Christlieb, N.; Wang, L.; Wang, W.; Zhang, Y.; Hou, Y.; Yuan, H. Spectroscopic Analysis of Metal-poor Stars from LAMOST: Early Results. *Astrophys. J.* **2015**, *798*, 110. [CrossRef]
74. Zhao, G.; Chen, Y. Low-*α* metal-rich stars with sausage kinematics in the LAMOST survey: Are they from the Gaia-Sausage-Enceladus galaxy? *Sci. China Physics Mech. Astron.* **2021**, *64*, 239562. [CrossRef]